Experimental X-ray Charge Density Studies on the Binary Carbonyls $Cr(CO)_6$, $Fe(CO)_5$, and $Ni(CO)_4$

Louis J. Farrugia* and Cameron Evans

WestCHEM, Department of Chemistry, University of Glasgow, Glasgow G12 8QQ, Scotland, U.K.

Received: June 9, 2005; In Final Form: July 28, 2005

The experimental charge densities in the binary carbonyls $Cr(CO)_6$ (**1**), $Fe(CO)_5$ (**2**), and $Ni(CO)_4$ (**3**) have been investigated on the basis of high-resolution X-ray diffraction data collected at 100 K. The nature of the metal−ligand interactions has been studied by means of deformation densities and by topological analyses using the Atoms in Molecules (AIM) approach of Bader. A detailed comparison between the experimental results and theoretical results from previous work and from gas-phase and periodic DFT/B3LYP calculations shows excellent agreement, both on a qualitative and quantitative level. An examination of the kappa-restricted multipole model (KRMM) for $Cr(CO)_6$, using theoretically derived structure factors, showed it to provide a somewhat worse fit than a model with freely refined κ' values. The experimental atomic graphs for the metal atoms in **2** and **3** were found to be dependent on the multipole model used for that atom. In the case of compound **2**, restriction of the multipole populations according to idealized site symmetry of D_{3h} gave an atomic graph in essential agreement with the theoretical gas-phase study. For compound **3**, all multipole models fail to reproduce the atomic graph obtained from the theoretical gas-phase study. The atomic quadrupole moments for the C atoms in all compounds were consistent with significant π back-donation from the metal atoms.

1. Introduction

The binary transition-metal carbonyls $Cr(CO)_6$ (**1**), $Fe(CO)_5$ (**2**), and $Ni(CO)_4$ (**3**) are among the most studied organometallic molecules—the literature on their chemical properties and bonding is vast.[1] They are prototypical examples illustrating the bonding of CO to zerovalent transition metals, in molecules with (idealized) O_h, D_{3h}, and T_d symmetry, respectively. There have been numerous theoretical[2,3] investigations, dating back decades, into their electronic structures, binding and dissociation energies, and reactivity, and these compounds have often been used as test examples for the ab initio post Hartree−Fock quantum mechanical treatment of transition-metal molecules. It is only relatively recently however, with the general acceptance of Density Functional Theory (DFT)[4] and the use of effective core potentials,[5] that reasonably accurate bond energies, geometries, and electron densities have become easily available for transition-metal complexes.

The seminal importance of molecules **1**−**3** led to early X-ray[6] and gas-phase electron diffraction[7] structure determinations. Later work by Rees and Mitschler[8] and Braga et al.[9] provided more precise X-ray derived geometric data. Most theoretical studies on metal carbonyls have focused on interpretations of the wave function through analysis of the molecular orbitals,[2,3] and much attention has been paid to the relative extent of σ-donation and π back-donation involving the CO ligands. However, the Atoms in Molecules (AIM) methodology of Bader[10] offers another vantage point, through analysis of the total electron density, and it is increasingly being used to gain new perspectives on chemical bonding. The gradient of the density $\nabla\rho(\boldsymbol{r})$ exhibits critical points (cp's) where this value is zero. Where the curvatures in three dimensions are all negative, at the (3,−3) cp, the density is at a maximum—this is the attractor which is normally at or near an atomic nucleus. Especially important are the (3,−1) cp's, or bond cp's, which are almost always associated with conventional covalent chemical bonds. The line starting at one of these bcp's and following the path of steepest ascent terminates at the attractor and is known as a bond path. According to Bader,[11] such a bond path unequivocally characterizes a chemical bond in the AIM approach, though this has recently[12] been questioned. Another important concept is the interatomic (or zero-flux) surface, which is defined such that at every point **r** on the surface, the normal **n** to the surface is orthogonal to $\nabla\rho(\boldsymbol{r})$, i.e. $\mathbf{n} \cdot \nabla\rho(\boldsymbol{r}) = 0$. This surface defines the boundary condition for application of quantum mechanics to an open system—to atoms in molecules.[10] It leads to a unique partitioning of space, and integration of properties such as the electron population within this surface leads to an unambiguous definition of atomic charge.

The first theoretical AIM study on molecules **1**−**3** was reported by MacDougall and Hall[13] in 1990. This work, investigating the Laplacian of the density $\nabla^2\rho(\boldsymbol{r})$, showed the characteristic [8,12,6] "cuboidal" atomic graph for the octahedrally coordinated Cr atom, which exemplifies the "lock and key" concept[10] of the donor−acceptor Cr−CO bond. More recently, Macchi and Sironi[14] and Cortés-Guzmán and Bader[15] have analyzed the bonding in molecules **1**−**3** from an AIM viewpoint in two detailed reviews. The large charge concentrations on the carbon atoms match the charge depletions on the Cr center (see Figure 4 of ref 14 or Figure 8 of ref 15). A similar situation is found for $Fe(CO)_5$ with respect to the two *axial* CO ligands, though the charge concentrations of the *equatorial* CO ligands avoid the charge depletions on the Fe center. For $Ni(CO)_4$, with a formal d^{10} configuration, there is a tetrahedral arrangement of four, much less pronounced, charge concentrations which face the charge concentrations of the CO ligands.[13]

* Corresponding author fax: +441413304888; e-mail: louis@chem.gla.ac.uk.

10.1021/jp053107n CCC: $30.25
Published on Web 09/10/2005

TABLE 1. Crystallographic Experimental Details[a]

compound formula	C_6CrO_6	C_5FeO_5	C_4NiO_4
compound color	colorless	yellow	colorless
M_r	220.06	195.9	170.75
space group	*Pnma* (no. 62)	*C*2/*c* (no. 15)	*P* a-3 (no. 205)
crystal system	orthorhombic	monoclinic	cubic
a/Å	11.5259(1)	11.6748(6)	10.7056(3)
b/Å	10.9394(1)	6.7759(3)	
c/Å	6.2162(1)	9.2419(4)	
β/deg		107.824(2)	
V/Å^{-3}	783.78(2)	696.01(6)	1226.97(6)
Z	4	4	8
D_{calc}/g cm^{-3}	1.865	1.87	1.849
F(000)	432	384	672
λ/Å	0.71073	0.71073	0.71073
μ(Mo$-K_a$)/mm^{-1}	1.451	2.132	3.094
crystal size/mm	0.30 × 0.32 × 0.38	0.28 × 0.28 × 0.60	0.28 × 0.28 × 0.60
transmission coefficients (range)	0.633−0.776	0.4231−1.0	0.3106−1.0
θ range/deg	3.54−55.13	3.52−50.04	3.3−45.27
$\sin(\theta_{max})/\lambda$	1.154	1.0788	1.00
no. of data used for merging	61787	110931	154363
no. of unique data	5179	3676	1721
hkl range	−26 → 23; −25 → 25; −14 → 14	−25 → 25; −14 → 14; −19 → 19	−21 → 21; −21 → 21; −21 → 21
R_{int}	0.0260	0.0418	0.0359
R_σ	0.0128	0.0116	0.0106
	spherical atom refinement		
no. of data in refinement	5179	3676	1721
no. of refined parameters	68	52	28
final $R[I > 2\sigma(I)]$ (all data)	0.0194 (0.021)	0.0208 (0.0228)	0.0178 (0.0230)
$R_w^2[I > 2\sigma(I)]$ (all data)	0.06 (0.0606)	0.0579 (0.0588)	0.055 (0.0562)
goodness of fit *S*	1.155	1.055	1.317
largest remaining feature in	0.803(max)	0.711(max)	0.409 (max)
electron density map/ eÅ^{-3}	−0.849(min)	−0.731(min)	−0.308 (min)
max shift/esd in last cycle	0.001	<1.0e-3	<1.0e-3
	multipole refinement		
no. of data in refinement	3999	3406	1467
no. of refined parameters	195	112	55
final $R[I > 3\sigma(I)]$ (all data)	0.0092(0.0139)	0.0120(0.0154)	0.0117(0.0207)
$R_w[I > 3\sigma(I)]$	0.0117	0.0126	0.0137
goodness of fit *S*	1.684	1.758	1.939
largest remaining feature in	0.211(max)	0.179(max)	0.250(max)
electron density map/eÅ^{-3}	−0.126(min)	−0.120(min)	−0.194(min)
max shift/esd in last cycle	<1.0e-6	<1.0e-5	<1.0e-5

[a] $R = \Sigma(|F_o| - |F_c|)/\Sigma(F_o)$; $R_w = \{\Sigma(w(F_o - F_c)^2)/\Sigma(w(F_o)^2)\}^{1/2}$; $R_w^2 = \{\Sigma(w(F_o^2 - F_c^2)^2)/\Sigma(w(F_o^2)^2)\}^{1/2}$; $R_\sigma = \Sigma[\sigma(F_o^2)]/\Sigma[F_o^2]$; $R_{int} = \Sigma\{n/(n-1)\}^{1/2}|F_o^2 - F_o^2(\text{mean})|/\Sigma F_o^2$ (summation is carried out only where more than one symmetry equivalent is averaged).

One attractive feature of the AIM methodology is that it can equally be applied to experimentally derived electron densities, and it is now routinely used in experimental charge density studies.[16] Compound **1** has already been the subject of an experimental charge density study reported in 1976, in an era before AIM analysis was generally available. In this in-depth *X-N* diffraction study at 74 K, Rees and Mitschler[8] (hereafter RM) estimated the integrated charge on the Cr atom to be 0.15 ± 0.12 e. This small charge on the metal atom resulted from an average σ-donation of 0.35 e and a slightly larger π-back-donation of 0.38 e. At the time, they issued the caveat that all atomic charges "are necessarily arbitrary, as the concept of atoms in a molecule is itself ill-defined". With the development of AIM theory[10] this assertion is happily no longer the case. The deformation density clearly showed local charge depletions around the Cr atom in the directions of the carbonyl ligands (corresponding to the expected ligand field redistributions) as well as bonding charge concentrations between the Cr and C and C and O atoms. From the asphericity of the density around the Cr atom, it was concluded that the population ratio e_g:t_{2g} was 1:3. Some years later, Coppens and co-workers[16c,17] obtained a slightly smaller ratio of 1:2.4, based on a multipole refinement using the RM[8] experimental data.

Since $Fe(CO)_5$ and $Ni(CO)_4$ are highly toxic and liquid at ambient temperature, the difficulty in obtaining accurate single-crystal diffraction data is understandable. Herein we report high-resolution X-ray diffraction studies on molecules **1**−**3**, obtained using a diffractometer equipped with a CCD area detector and a laboratory X-ray source. We examine the experimental charge densities within the AIM methodology and compare their topological parameters, on a qualitative and quantitative level, with those obtained from theoretical reference densities and the previously reported[13−15] theoretical topological studies.

2. Experimental Section

Data Collection, Processing, and Spherical Atom Refinement. Compounds **1**−**3** were obtained from commercial sources and purified either by sublimation (**1**) or by vacuum distillation (**2** and **3**). For **1**, a single crystal of suitable size was attached to a glass fiber using silicone grease and mounted on a goniometer head in a general position. The crystal was cooled from ambient temperature to 100 K over a period of 1 h, using an Oxford Instruments Cryostream. Single crystals of **2** and **3** were grown directly on the diffractometer by repeated freeze−thaw cycles on the pure liquid contained in a 0.3 mm capillary.

Details of data collection procedures are given in Table 1. Data were collected on an Bruker-Nonius KappaCCD diffractometer, running under Nonius Collect software.[18a] The Collect software calculates and optimizes the goniometer and detector

angular positions during data acquisition. The oscillation axis was either the diffractometer ω- or φ-axis with scan angles of 1.7−2.0°. The short exposure scan sets were used to record the intense low-order data more accurately (absolute detector θ-offset for these scan sets was < 7°), since high-intensity diffraction spots are subject to pixel overflow or integration failure in the long exposure images. The scan sets with low detector θ-offsets were measured first in the data collection strategy, to alleviate problems with ice-rings which gradually build up during data collection. The high angle images showed no evidence of contamination from ice-rings. The unit cell dimensions used for refinement purposes were determined by postrefinement of the setting angles of a significant portion of the data set, using the Scalepack program.[18b] The cell errors obtained from this least-squares procedure are undoubtedly serious underestimates[19] but are used here in the absence of better estimates.

The frame images were integrated using Denzo(SMN).[18b] As we have recently shown,[20] the neighborhood profiling used in Denzo(SMN)[18b] appears to cope quite well with the problem of $K_{\alpha 1\text{-}\alpha 2}$ splitting, provided a sufficiently large integration spot size is chosen. The resultant raw intensity files from Denzo-(SMN) were processed using a locally modified version of DENZOX.[21] Frame to frame scaling was then applied using SADABS[22a] to account for the differing image exposure times and for machine instability factors such as shutter inaccuracies or goniometer slippage, and a semiempirical correction[23] was applied, to remove absorption anisotropy from the crystal and any residual absorption anisotropy due to the mounting medium. No significant variations in scale factors with accumulated X-ray exposure time were noted for any sample, indicating no decomposition or evaporation. The scale factors reported by SADABS are normalized scale factors, such that the average scale factor within a scan-set is unity. They therefore do not reflect the scaling factors due to the different image exposure times. Systematically absent reflections were removed, and the data were sorted and merged using SORTAV.[24] A spherical atom refinement using SHELXL97-2[25] was initially undertaken, with full-matrix least-squares on F^2 and using all the unique data. All atoms were allowed anisotropic thermal motion. Neutral atom scattering factors, coefficients of anomalous dispersion, and absorption coefficients were obtained from ref 26. Details of these refinements are given in Table 1. Thermal ellipsoid plots were obtained using the program ORTEP-3 for Windows.[27] All calculations were carried out using the WinGX package[28] of crystallographic programs.

The sample configuration of a frozen crystal in a capillary tube introduces two additional sources of error in the measurement of structure factors: (i) the differential sample-volume irradiated and (ii) an additional absorption by the capillary of those reflections whose scattering vector is parallel, or nearly parallel, to the capillary axis (essentially the goniometer φ axis). The former effect is quite significant but is a smoothly varying function of the goniometer ω and χ angles and appears to be very adequately modeled by the SADABS[22a] program. The corrections applied by the program for this effect (Figure S1) are well within the expected limits. The latter source of error is due to additional absorption through the tip of the capillary and is visible as a "shadow" on those images where the φ axis vector crosses the detector. This problem could not be corrected explicitly, as the corresponding mask for the integration software is not available. Nevertheless, we assume, given the very high redundancies for these two samples (Figure S2), that any outliers arising from this effect are either eliminated or make a small contribution to the averaged intensity in the merging process. The maximum dimension of the crystal is given in Table 1 as notionally 0.6 mm, this being the estimated length of the capillary exposed to a homogeneous X-ray beam. The actual length of the crystal is considerably longer.

Specific Details for $Cr(CO)_6$. A total of 1346 frame images in 20 scan sets were measured over a time period of 80.4 h. An integration time of 8.5 s was used for scan sets #1−8 and 170 s for the remaining scan sets. A total of 66 853 intensity measurements were harvested from the image files. An absorption correction by Gaussian quadrature,[29] based on the measured crystal faces, was then applied to the reflection data, giving a range of transmission factors of 0.633−0.776. Frame-to-frame scaling using SADABS[22a] gave relative scale factors in the range 1.0−0.801. A theta dependent correction with SADABS was not applied for this data set. The resulting 61 787 data were merged with SORTAV,[24] giving a total of 5179 independent data, with a mean redundancy of 12.0. The data set is 99.3% complete for $0 < \theta \leq 55.3°$ and has just 2 reflections missing in the range $0 < \theta \leq 51.2°$. Data were originally indexed and integrated using the reduced primitive orthorhombic cell (space group *Pcmn*), and all data processing as described above was carried out using this indexing. To facilitate direct comparison with the analysis of RM,[8] the data were then transformed to the standard setting of *Pnma*, using the same atomic numbering scheme and coordinates as RM. A scatter-plot of the scale factor between observed and calculated F as a function of $\sin(\theta)/\lambda$ (Figure S3) showed that the highest resolution data above $\sin(\theta)/\lambda > \sim 1.1$ Å^{-1} were slightly underestimated, so the data set used for this study was truncated at $\theta_{max} = 50.0°$.

Specific Details for $Fe(CO)_5$. A total of 4605 frame images in 83 scan sets were measured over a time period of 96.3 h. Integration times of 4.0, 40.0, and 140.0 s per image were used in the various scan sets. A total of 119 187 intensity measurements were harvested from the image files. An empirical correction using SADABS[22a] was then applied to the reflection data, giving a range of correction factors of 0.4231−1.0. The resulting 110 931 data were then sorted and merged yielding 3676 independent data, with a mean redundancy of 30.2. The data set is 100% complete for $0 < \theta \leq 50.0°$. The atomic coordinates and labeling scheme of Braga et al.[9] were used to initiate refinement.

Specific Details for $Ni(CO)_4$. A total of 2620 frame images in 51 scan sets were measured over a time period of 98.1 h. Integration times of 7.0, 70.0, and 234.0 s per image were used in the various scan sets. A total of 206 681 intensity measurements were harvested from the image files. An empirical correction using SADABS[22a] was then applied to the reflection data, giving a range of correction factors of 0.3106−1.0. As a result of relatively poor scattering at the highest angles, only those data with $\sin(\theta)/\lambda \leq 1.0$ were retained. The resulting 154 363 data were then merged, yielding 1721 independent data, with a mean redundancy of 89.7. The data set is 100% complete for $\sin(\theta)/\lambda \leq 1.0$. The data were then reindexed so that the atomic coordinates and labeling scheme of Braga et al.[9] could be used to initiate refinement.

Alternative Data Processing. To examine the possibility that the empirical "absorption" correction program SADABS[22a] introduced systematic errors, particularly affecting the single heavy metal-atom scatterer (see the section below on atomic graphs), the data for **2** were also processed using the program ABCYL.[22b] This program provides an analytical correction for the differential volume of irradiation and the sample absorption, using a simple approximation for the X-ray beam profile and

size. The program SORTAV was then used to provide frame scaling, an additional correction for absorption anisotropy, and data merging. The resultant data set showed slightly worse residuals than the SADABS processed data, and there were no significant differences in the derived atomic graph of the metal atom. Since the data set processed with SADABS gave better statistics, this one was used in the final refinements. The empirical frame scale-factors applied by SADABS (the "incident beam" corrections) closely follow the volume correction predicted by ABCYL (Figure S1).

Multipole Refinements. The multipole formalism of Hansen and Coppens[30] as implemented in the XD program suite[31] was used. The aspherical atomic electron density $\rho(\mathbf{r})$ is divided into three parts

$$\rho(\mathbf{r}) = \rho_c(\mathbf{r}) + P_v\kappa^3\rho_v(\kappa\mathbf{r}) + \rho_d(\kappa'\mathbf{r})$$

where ρ_c and ρ_v are respectively the core and spherical valence densities, and

$$\rho_d(\kappa'\mathbf{r}) = \sum_{l=0}\kappa^3 R_l(\kappa'\mathbf{r})\sum_{m=0}^{l} P_{lm\pm}y_{lm\pm}(\mathbf{r}/r)$$

is the term accounting for the deformation valence densities. The $y_{lm\pm}$ are density normalized, real spherical harmonics, and P_v, $P_{lm\pm}$ are the refinable populations. The function minimized in the least squares procedure was $\Sigma w(|F_o| - k|F_c|)^2$, with only those reflections with $I > 3\sigma(I)$ included in the refinement. The multipole expansion was truncated at the hexadecapole level for the metal atoms and at the octupole level for the C and O atoms. Each pseudoatom was assigned a core and spherical-valence scattering factor constructed from the relativistic Dirac−Fock wave functions of Su and Coppens[32] expanded in terms of the single-ζ functions of Bunge, Barrientos, and Bunge.[33] The radial fit of the valence density was optimized by refinement of the expansion-contraction parameter κ. The valence deformation functions for the C and O used a single-ζ Slater-type radial function multiplied by the density-normalized spherical harmonics. For the transition metals, the radial terms used were either simple Slater functions (for $l = 1,3$) or the relevant order Fourier-Bessel transforms of the Su and Coppens[32] wave functions for ($l = 0,2,4$). For all pseudoatoms, the valence-deformation radial fits were optimized by refinement of their expansion-contraction parameters κ', though for certain atoms this proved problematical (see below).

It is well established[17b] that the 3*d* transition metals present special problems when refining the deformation density because of the significantly different radial extensions of the 3*d* and 4*s* valence orbitals. In view of these problems, it is common practice to treat the 4*s* density as "core" density (i.e. include it as a fixed component), since the scattering from this density is only significant for sin $\theta/\lambda < 0.2$ and only a few reflections will contribute. The final model scattering factors were constructed from a $4s^13d^n$ configuration for Cr and $4s^23d^n$ configurations for Fe and Ni, since these gave better fits than trial $3d^n$ configurations. Attempts to refine the 4*s* population independently through the $l = 0$ deformation function (the second monopole) were unsuccessful; all such models proved unstable or gave physically unrealistic populations.

For $Cr(CO)_6$ two experimental multipole models are compared in this report: a model in which each individual atom had a unique κ' parameter which was freely refined (model A), and a kappa restricted multipole model (KRMM)[34] (model B) in which each elemental type was assigned a κ' parameter obtained from multipole refinements against theoretically derived structure factors (from periodic DFT/B3LYP calculations using a 6-31G* basis with the CRYSTAL98 program[35]). Finally, a theoretical model (model C) was obtained by projection of the density from the static theoretical structure factors into a multipole model. No thermal or positional parameters were refined in this latter model. In models C and A, each individual O and C atom used a unique κ' parameter, while in model B, one κ' parameter was used for all O atoms and one κ' parameter for all C atoms. The κ' parameters for model B were obtained from a slight variant of model C, in which each elemental type shared the same κ' parameter. For all three models, the same κ' parameter was used for all the valence-deformation multipoles (the KEEP KAPPA directive in XD), since refinements with individual κ' parameters for each *l* multipole proved unstable.

For $Fe(CO)_5$, two models were also examined in some detail. The first model contained only those restrictions on the multipole populations required by the C_2 crystallographic site symmetry. In the second model, constraints were applied to the multipole populations of all atoms consistent with strict D_{3h} molecular symmetry. Since this latter model provided only a slightly worse fit ($R(F) = 0.0120$. GOF = 1.76 compared with $R(F) = 0.0115$, GOF = 1.69), but with 48 fewer refined parameters, it was chosen as the final model. Sharp features near the Fe atom in the residual map (Figures S11 and S12a) indicated a possible anharmonicity, so this hypothesis was tested by adding third- and fourth-order Gram-Charlier coefficients for the Fe atom. The fit was significantly improved ($R(F) = 0.0125$ before and 0.0120 after introduction of anharmonicity), and the final residual map was quite featureless ($\Delta\rho$ maxima reduced from 0.245 to 0.179 eÅ^{-3}), so the anharmonic model was chosen as the final model. Since it is not always easy to distinguish anharmonicity from charge density effects, care was taken to ensure that the correlations between the anharmonic thermal parameters and the multipole parameters[36] were limited by refining them in separate blocks. The resultant probability density function was positive in all regions (Figure S4) and hence was physically meaningful. No anharmonicity was deemed necessary or was included for compounds **1** or **3**; the reason it was observed for **2** may be due to the lower site symmetry of the Fe atom. When freely refined, the κ' parameter of the O atoms for $Fe(CO)_5$ gave an unrealistically contracted value, so in the final model it was fixed at 1.0.

The crystallographic site symmetry in $Ni(CO)_4$ requires at least C_3 symmetry for the Ni atom multipoles. For this symmetry model, none of the multipole populations $y_{lm\pm}$ with $l > 0$ differ from zero by more than 2.5σ, and a model where all these populations are set to zero provides virtually as good a fit. This indicates that the experimental valence density is almost spherically symmetrical (see below). In the final model chosen, the multipole populations were restricted to T_d symmetry on the Ni atom and to C_3 symmetry on the C and O atoms. For the Ni atom, only the multipoles P_{00}, P_{32-}, and the kubic harmonic K_{41} (a linear combination of P_{40} and P_{44+}) are allowed. The local axial system is aligned with the crystallographic axes, i.e. parallel to the S_4 axes bisecting the C−Ni−C bonds. Since the multipole populations on Ni are very small, the associated κ' parameter is a weak one in the least-squares, and refinement of this parameter proved unstable. The value used in the final model was optimized by refinements with several fixed values. The κ' parameter of the O atom in $Ni(CO)_4$ was treated as for $Fe(CO)_5$. The κ and κ' parameters used for all three structures are listed in Table 2.

TABLE 2. κ and κ' Parameters

	κ	κ'
Cr[a]	1.181(9)	1.11(2)
	1.178(9)	0.95
	1.058	0.95
O[b]	1.01(8)	0.86(18)
	1.014(16)	1.19
	0.988(2)	1.20(3)
C[b]	1.026(7)	0.90(5)
	1.017(8)	0.86
	1.00(1)	0.87(1)
Fe	0.975(3)	1.04(2)
O	1.006(1)	1.0
C	0.991(2)	0.927(4)
Ni	0.976(9)	1.1
O	1.005(5)	1.0
C	0.996(8)	0.905(6)

[a] For $Cr(CO)_6$, the first line shows values for model A, the second line for model B, and the third line for multipole refinement against theoretical static structure factors. [b] Averaged values for C and O atoms.

For all three structures, an adequate deconvolution of the thermal motion from the bonding density was judged from the rigid-bond criterion of Hirshfeld.[37] The mean and largest Δ-msda values were respectively 6 and 14 $\times 10^{-4}$ Å^2, with the largest value being that for Cr−C(2). As is often observed for metal−ligand bonds,[38] the mean Δ-msda for the M−C bonds (1×10^{-3} Å^2) was greater than for the C−O bonds (2×10^{-4} Å^2). This may reflect some inadequacy in the radial functions used for the metal atoms, incomplete deconvolution of the thermal parameters, or a breakdown in the applicability of the Hirshfeld criterion for heavy-atom/light-atom bonds. The final difference Fourier maps (Table 1 and Supporting Information Figures S5, S13, and S20) show features in the range +0.25 to −0.2 eÅ^{-3} over the three structures. The maxima are in the vicinity of the metal atoms.

The kinetic energy densities at the bcp's $G(\mathbf{r})$ given in Tables 3−5 for the experimental densities were estimated using the functional approximation of Abramov[39]

$$G(\mathbf{r}) = (3/10)(3\pi^2)^{2/3}\rho(\mathbf{r})^{5/3} + (1/6)\nabla^2\rho(\mathbf{r})$$

while the corresponding potential energy densities at the bcp's $V(\mathbf{r})$ were obtained from

$$V(\mathbf{r}) = (1/4)\,\nabla^2\rho(\mathbf{r}) - 2G(\mathbf{r})$$

The approximation[39] for $G(\mathbf{r})$ holds well for closed shell interactions, where $\nabla^2\rho(\mathbf{r}) > 0$, and is a good approximation for all the covalent bonds in $Cr(CO)_6$ (see below).

Integrated atomic properties were obtained using the TOPXD program.[31,40] The accuracy of integration can be gauged[40] by the magnitude of the integrated atomic Lagrangian function $L(\Omega) = -(1/4)\int_\Omega \nabla^2\rho(\mathbf{r})d\tau$, which should vanish according to the atomic basin boundary conditions. Apart from the atom Fe(1) ($L(\Omega) = 1.2 \times 10^{-3}$ au), these were all below 1.0×10^{-3} au, which is considered reasonable.[40] The summed atomic volumes were in agreement with the unit cell volumes to better than 99.8%. Errors on properties are not computed by the program, though a number of studies[40,41] suggest a conservative estimate of $\sim \pm 5\%$ for the *accuracy* of the integrated atomic properties, though some properties, e.g. electron populations, are much less sensitive to errors than others.

Theoretical Studies. Reference densities were obtained from gas-phase, single point DFT (B3LYP) calculations, using a

TABLE 3. Topological Analysis of Bond Critical Points for $Cr(CO)_6$[a]

bond	R_b[b]	d1[b]	d2[b]	$\rho(\mathbf{r_b})$[c]	$\nabla^2\rho(\mathbf{r}_b)$[d]	λ_1[d]	λ_2[d]	λ_3[d]	ϵ	$G(\mathbf{r}_b)$[e,f]	$G(\mathbf{r}_b)/\rho(\mathbf{r}_b)$	$V(\mathbf{r}_b)$[e]	$E(\mathbf{r}_b)$[e]
Cr−C(1)	1.9108	0.9488	0.9620	0.700(3)	13.263(6)	−2.68	−2.66	18.60	0.01	1.06	1.52	−1.20	−0.13
	1.9106	0.9424	0.9682	0.694(2)	14.106(5)	−2.30	−2.25	18.66	0.02	1.10	1.58	−1.20	−0.11
	1.9120	*0.9397*	*0.9723*	*0.675*	*14.976*	*−1.90*	*−1.52*	*18.40*	*0.25*	*1.12*	*1.65*	*−1.18*	*−0.07*
	1.9109	*0.9472*	*0.9637*	*0.731*	*11.851*	*−2.29*	*−2.29*	*16.43*	*0.00*	*1.03*	*1.41*	*−1.23*	*−0.20*
Cr−C(2)	1.9153	0.9563	0.9590	0.679(3)	12.878(6)	−2.56	−2.38	17.82	0.08	1.02	1.51	−1.14	−0.12
	1.9159	0.9532	0.9626	0.655(3)	13.789(5)	−2.21	−2.04	18.04	0.09	1.04	1.59	−1.12	−0.09
	1.9164	*0.9436*	*0.9728*	*0.695*	*14.763*	*−2.04*	*−1.85*	*18.65*	*0.10*	*1.13*	*1.62*	*−1.22*	*−0.09*
	1.9149	*0.9486*	*0.9663*	*0.724*	*11.768*	*−2.26*	*−2.25*	*16.27*	*0.00*	*1.02*	*1.41*	*−1.21*	*−0.20*
Cr−C(3)	1.9141	0.9490	0.9651	0.679(4)	13.190(6)	−2.50	−2.42	18.11	0.03	1.04	1.53	−1.15	−0.11
	1.9141	0.9435	0.9705	0.667(4)	14.204(5)	−2.17	−2.12	18.49	0.02	1.07	1.61	−1.15	−0.09
	1.9146	*0.9415*	*0.9730*	*0.696*	*14.799*	*−1.94*	*−1.89*	*18.63*	*0.03*	*1.13*	*1.62*	*−1.22*	*−0.09*
	1.9141	*0.9483*	*0.9658*	*0.726*	*11.673*	*−2.35*	*−2.25*	*16.28*	*0.04*	*1.02*	*1.41*	*−1.22*	*−0.20*
Cr−C(4)	1.9185	0.9494	0.9691	0.671(4)	12.968(6)	−2.54	−2.50	18.01	0.02	1.02	1.52	−1.13	−0.11
	1.9187	0.9427	0.9760	0.675(4)	13.846(5)	−2.27	−2.21	18.33	0.03	1.06	1.58	−1.16	−0.09
	1.9185	*0.9420*	*0.9766*	*0.685*	*14.895*	*−1.87*	*−1.75*	*18.51*	*0.07*	*1.12*	*1.64*	*−1.20*	*−0.08*
	1.9184	*0.9495*	*0.9689*	*0.720*	*11.588*	*−2.33*	*−2.23*	*16.14*	*0.04*	*1.01*	*1.40*	*−1.21*	*−0.20*
O(1)−C(1)	1.1430	0.7513	0.3917	3.419(13)	−8.770(88)	−36.82	−36.16	64.21	0.02	5.83	1.71	−12.27	−6.44
	1.1429	0.7541	0.3888	3.307(1)	−0.016(56)	−34.53	−34.19	68.70	0.01	5.90	1.78	−11.80	−5.90
	1.1430	*0.7522*	*0.3907*	*3.310*	*−9.615*	*−38.33*	*−33.39*	*62.10*	*0.15*	*5.46*	*1.65*	*−11.60*	*−6.14*
	1.1429	*0.7501*	*0.3928*	*3.266*	*2.443*	*−35.61*	*−35.61*	*73.65*	*0.00*	*6.33*	*1.94*	*−12.49*	*−6.16*
O(2)−C(2)	1.1426	0.7521	0.3905	3.347(12)	−3.636(70)	−35.87	−33.87	66.10	0.06	5.85	1.75	−11.96	−6.11
	1.1422	0.7481	0.3941	3.367(7)	−10.094(55)	−35.66	−33.71	59.27	0.06	5.61	1.67	−11.93	−6.32
	1.1424	*0.7479*	*0.3945*	*3.201*	*−8.370*	*−34.68*	*−32.27*	*58.58*	*0.07*	*5.20*	*1.62*	*−10.99*	*−5.79*
	1.1424	*0.7498*	*0.3926*	*3.270*	*2.578*	*−35.67*	*−35.67*	*73.93*	*0.00*	*6.35*	*1.94*	*−12.52*	*−6.17*
O(3)−C(3)	1.1419	0.7494	0.3925	3.408(12)	−9.620(87)	−35.60	−35.25	61.23	0.01	5.76	1.69	−12.19	−6.43
	1.1416	0.7501	0.3914	3.383(10)	−7.590(77)	−35.24	−34.70	62.35	0.02	5.78	1.71	−12.08	−6.31
	1.1420	*0.7486*	*0.3933*	*3.346*	*−12.665*	*−35.66*	*−34.87*	*57.86*	*0.02*	*5.43*	*1.62*	*−11.74*	*−6.31*
	1.1419	*0.7494*	*0.3925*	*3.274*	*2.688*	*−35.75*	*−35.75*	*74.18*	*0.00*	*6.37*	*1.95*	*−12.54*	*−6.18*
O(4)−C(4)	1.1404	0.7446	0.3958	3.410(17)	−11.77(12)	−35.59	−34.23	58.04	0.04	5.66	1.66	−12.15	−6.49
	1.1399	0.7486	0.3913	3.336(10)	−2.473(80)	−33.98	−32.63	64.14	0.04	5.87	1.76	−11.92	−6.05
	1.1404	*0.7477*	*0.3926*	*3.356*	*−13.404*	*−36.87*	*−34.80*	*58.27*	*0.06*	*5.42*	*1.62*	*−11.78*	*−6.36*
	1.1404	*0.7484*	*0.3920*	*3.285*	*3.038*	*−35.98*	*−35.98*	*75.00*	*0.00*	*6.42*	*1.95*	*−12.63*	*−6.21*

[a] For each entry, first line experimental values (model A), second line experimental values (model B), third line multipole model with theoretical structure factors, fourth line theoretical values from isolated molecule DFT calculation. [b] In units of Å. [c] In units of e Å^{-3}. [d] In units of e Å^{-5}. [e] In units of Hartree Å^{-3}. [f] Estimated by the approximation of Abramov.[39]

TABLE 4. Topological Analysis of Bond Critical Points for $Fe(CO)_5$[a]

bond	R_b[b]	d1[b]	d2[b]	$\rho(\mathbf{r}_b)$[c]	$\nabla^2\rho(\mathbf{r}_b)$[d]	λ_1[d]	λ_2[d]	λ_3[d]	ϵ	$G(\mathbf{r}_b)$[e,f]	$G(\mathbf{r}_b)/\rho(\mathbf{r}_b)$	$V(\mathbf{r}_b)$[e]	$E(\mathbf{r}_b)$[e]
Fe−C(1)	1.8131	0.9353	0.8778	0.965(8)	12.463(14)	−4.67	−4.41	21.54	0.06	1.34	1.39	−1.81	−0.47
	1.8129	*0.9289*	*0.8840*	*0.943*	*12.659*	*−4.16*	*−4.01*	*20.82*	*0.04*	*1.23*	*1.31*	*−1.58*	*−0.35*
Fe−C(2)	1.8187	0.9014	0.9173	0.897(9)	14.45(2)	−3.56	−3.54	21.45	0.00	1.34	1.49	−1.68	−0.34
	1.8187	*0.9022*	*0.9185*	*0.884*	*13.495*	*−3.08*	*−3.08*	*19.65*	*0.00*	*1.24*	*1.41*	*−1.54*	*−0.30*
Fe−C(3)	1.8098	0.9328	0.8770	0.994(7)	12.111(12)	−4.97	−4.70	21.78	0.06	1.36	1.37	−1.87	−0.51
	1.8129	*0.9289*	*0.8840*	*0.943*	*12.659*	*−4.16*	*−4.01*	*20.82*	*0.04*	*1.23*	*1.31*	*−1.58*	*−0.35*
O(1)−C(1)	1.1451	0.7489	0.3962	3.378(14)	−18.4(2)	−36.76	−35.69	54.05	0.03	5.26	1.56	−11.80	−6.54
	1.1467	*0.7528*	*0.3939*	*3.236*	*1.836*	*−34.92*	*−34.73*	*71.49*	*0.01*	*6.22*	*1.92*	*−12.30*	*−6.09*
O(2)−C(2)	1.1387	0.7417	0.3970	3.43(3)	−19.4(2)	−36.29	−36.29	53.17	0.00	5.35	1.56	−12.06	−6.71
	1.1382	*0.7464*	*0.3918*	*3.301*	*3.308*	*−35.76*	*−35.76*	*74.82*	*0.00*	*6.48*	*1.96*	*−12.73*	*−6.25*
O(3)−C(3)	1.1444	0.7524	0.3919	3.35(2)	−6.80(14)	−35.06	−33.39	61.65	0.05	5.71	1.71	−11.90	−6.19
	1.1467	*0.7528*	*0.3939*	*3.236*	*1.836*	*−34.92*	*−34.73*	*71.49*	*0.01*	*6.22*	*1.92*	*−12.30*	*−6.09*

[a] Top line experimental values, second line theoretical values from isolated molecule DFT calculation. [b] In units of Å. [c] In units of e Å^{-3}. [d] In units of e Å^{-5} [e] In units of Hartree Å^{-3}. [f] Estimated by the approximation of Abramov.[39]

TABLE 5. Topological Analysis of Bond Critical Points for $Ni(CO)_4$[a]

bond	R_b[b]	d1[b]	d2[b]	$\rho(\mathbf{r}_b)$[c]	$\nabla^2\rho(\mathbf{r}_b)$[d]	λ_1[d]	λ_2[d]	λ_3[d]	ϵ	$G(\mathbf{r}_b)$[e,f]	$G(\mathbf{r}_b)/\rho(\mathbf{r}_b)$	$V(\mathbf{r}_b)$[e]	$E(\mathbf{r}_b)$[e]
Ni−C(1)	1.8283	0.9346	0.8937	0.913(4)	11.141(6)	−4.42	−4.42	19.97	0.00	1.21	1.33	−1.64	−0.43
	1.8275	*0.9223*	*0.9052*	*0.869*	*13.354*	*−3.73*	*−3.73*	*20.82*	*0.00*	*1.21*	*1.39*	*−1.49*	*−0.28*
Ni−C(2)	1.8249	0.9299	0.8951	0.944(8)	11.316(13)	−4.65	−4.65	20.61	0.00	1.26	1.33	−1.72	−0.47
	1.8275	*0.9223*	*0.9052*	*0.869*	*13.354*	*−3.73*	*−3.73*	*20.82*	*0.00*	*1.21*	*1.39*	*−1.49*	*−0.28*
O(1)−C(1)	1.1392	0.7469	0.3923	3.447(12)	−13.3(1)	−36.01	−36.01	58.76	0.00	5.71	1.66	−12.34	−6.63
	1.1386	*0.7476*	*0.3910*	*3.302*	*3.378*	*−36.68*	*−36.68*	*76.75*	*0.00*	*6.49*	*1.97*	*−12.74*	*−6.25*
O(2)−C(2)	1.1376	0.7501	0.3875	3.466(3)	−9.5(2)	−38.65	−38.65	67.84	0.00	5.95	1.71	−12.54	−6.60
	1.1386	*0.7476*	*0.3910*	*3.302*	*3.378*	*−36.68*	*−36.68*	*76.75*	*0.00*	*6.49*	*1.97*	*−12.74*	*−6.25*

[a] Top line gives experimental values, second line gives theoretical values from isolated molecule DFT calculation. [b] In units of Å. [c] In units of e Å^{-3} [d] In units of e Å^{-5}. [e] In units of Hartree Å^{-3}. [f] Estimated by the approximation of Abramov.[39]

6-311G+(2d) basis for C, O, and Wachters(+f) basis for the metal atoms with the GAMESS-UK program.[42] Basis sets were obtained from EMSL.[43] Atomic properties were obtained from these theoretical densities using a locally modified version of the AIMPAC programs[44] or AIM2000.[45] For $Cr(CO)_6$, calculations were undertaken at the experimental C_s geometry and also under O_h symmetry using both an optimized geometry and the averaged experimental geometry. In all cases, the topological and integrated properties were very similar and essentially identical to the previously reported calculations[14,15] on O_h geometry optimized models using the Gaussian98 code. The calculations reported herein are based on the experimental C_s geometry. For $Fe(CO)_5$ and $Ni(CO)_4$, the results reported are based on calculations with geometry optimized D_{3h} and T_d models, respectively. Periodic DFT/B3LYP calculations based on the experimental crystal structures were performed using the CRYSTAL98 or CRYSTAL03[35] program packages. Standard 6-31G* bases[43] were used for all atoms, except in $Fe(CO)_5$ and $Ni(CO)_4$, where the *f* polarization functions on the metals were removed to aid convergence. Static structure factors were computed from the resultant wave functions and used in refinements with XD, where all thermal parameters were set to zero and all positional parameters were fixed. Arbitrary standard uncertainties for the F_{hkl} values were chosen to give a goodness of fit between 1.0 and 2.0 and were typically ∼0.4% of the value of F_{hkl}.

Results and Discussion

Description of the Structures. The ORTEP plots and atomic labeling schemes for molecules **1**−**3** are shown in Figures 1−3. The metrical parameters in Table 6 are taken from the final multipole refinements and are compared with the previous accurate diffraction studies. The precision in this study is about an order of magnitude better than in the previous work, and we suggest these values may be used as the experimental values when calibrating accurate quantum calculations.

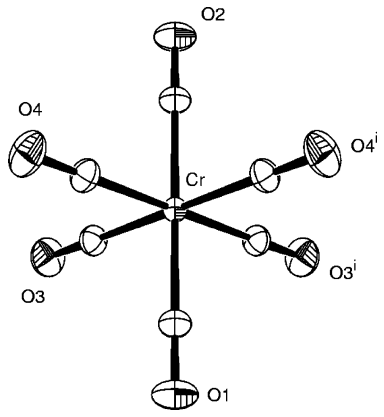

Figure 1. Ortep plot of $Cr(CO)_6$ (**1**) (80% probability ellipsoids) showing atomic labeling scheme. Primed atoms are related to unprimed atoms by the symmetry operation x, $^1/_2-y$, z.

Molecules **1**−**3** have crystallographic site symmetries (C_s, C_2, and C_3, respectively) which are all lower than their idealized molecular symmetries. The metrical parameters for $Cr(CO)_6$ agree within error with those of RM,[8] and deviations from idealized O_h symmetry are very small. The mean Cr−C and C−O distances are 1.915(7) and 1.142(2) Å (3.669 and 2.158 au), respectively, while the librationally corrected mean distances are 1.918(7) and 1.144(2) Å, respectively. The bond lengths for $Fe(CO)_5$ and $Ni(CO)_4$ are larger, by about 0.01 Å, than in the study of Braga et al.[9] This difference is too great to be associated with the known problem[46] of inaccuracies in the unit cell determination with area detector data. The difference between the mean $Fe-C_{eq}$ distance (1.812(3) Å, 3.423 au) and the $Fe-C_{ax}$ distance (1.8187(3) Å, 3.437 au) is 0.007 Å, in agreement with the results of Braga et al.[9] The mean distances for $Ni(CO)_4$ are Ni−C = 1.827(3) and C−O = 1.138(1) Å (3.452 and 2.151 au, respectively), and the deviation from exact T_d symmetry is very small.

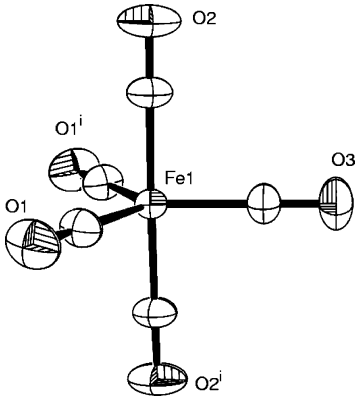

Figure 2. Ortep plot of $Fe(CO)_5$ (**2**) (80% probability ellipsoids) showing atomic labeling scheme. Primed atoms are related to unprimed atoms by the symmetry operation $-x, y, {}^1/_2-z$.

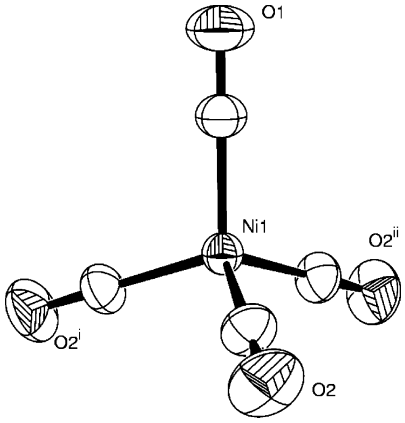

Figure 3. Ortep plot of $Ni(CO)_4$ (**3**) (80% probability ellipsoids) showing atomic labeling scheme. Primed atoms are related to unprimed atoms by the symmetry operation *y*, *z*, *x* and double primed atoms by the operation *z*, *x*, *y*.

It is clear, that in the solid-state structure at least, $Fe(CO)_5$ has an $Fe-C_{ax}$ bond which is just marginally longer than the $Fe-C_{eq}$ bond. This result is reproduced well in DFT calculations,[3e,3l,l4,15] but some more sophisticated quantum mechanical approaches which include correlation, such as multireference CI[3d] or CASPT2,[3m] predict the opposite order. The optimized geometries from quantum calculations on $Fe(CO)_5$ are often compared with the 1974 gas-phase experimental data,[7a] where the order is the opposite to that found for the solid, with $Fe-C_{eq} = 1.827(3)$ and $Fe-C_{ax} = 1.807(3)$ Å. A redetermination of the gas-phase structure may resolve this discrepancy between the experimental structures, though we note that a more recent electron diffraction study on the related molecule $Ru(CO)_5$ also shows[7c] the axial Ru−C bond to be shorter by 0.02 Å. The gas-phase structure determination[7b] for $Ni(CO)_4$ gave results in reasonable agreement (Ni−C = 1.832(2), C−O = 1.141(2) Å) with the current study.

Topological Analyses of ρ. The experimental density $\rho(\mathbf{r})$, as obtained from the multipole formalism of Hansen and Coppens,[30] was analyzed using the AIM approach of Bader.[10] The results are summarized in Tables 3−5, and plots of the residual densities, experimental and model deformation maps, and Laplacian maps in selected planes are given in Supporting Information Figures S5−S27. All the expected (3,−1) critical points (bond cp's) and bond paths, corresponding to the M−C and C−O covalent bonds, were observed. The experimental molecular graphs shown in Figure 4 are essentially identical to the theoretical graphs illustrated in Figure 2, ref 15, so there is an excellent qualitative agreement concerning the chemical bonding in these molecules. As outlined above, two experimental multipole models were examined for $Cr(CO)_6$. In model A, the κ' parameters were allowed to freely refine, while in model B, they were fixed at values obtained by refinement against theoretical structure factors (i.e. the KRMM[34]). In addition, a theoretical multipole model (model C) was obtained by refinement of a multipole model using XD[31] against the set of static structure factors. The results from models B and C are also included in Tables 2 and 3. The values for the κ' parameters of the C and O atoms obtained by refinement against the theoretical structure factors of $Cr(CO)_6$ are very similar to the values of 0.86(1) for C and 1.18(5) for O obtained by Coppens and coworkers[34a] for the carbonyl functional group in organic molecules.

TABLE 6. Bond Lengths (Å) and Bond Angles (deg)

	this work	previous work[a]
	$Cr(CO)_6$	
Cr−C(1)	1.9108(2)	1.9116(19)
Cr−C(2)	1.9149(2)	1.9160(20)
Cr−C(3)	1.91401(16)	1.9147(13)
Cr−C(4)	1.91838(18)	1.9180(13)
C(1)−O(1)	1.1429(3)	1.1426(26)
C(2)−O(2)	1.1424(3)	1.1411(28)
C(3)−O(3)	1.1419(3)	1.1390(19)
C(4)−O(4)	1.1403(3)	1.1380(19)
Cr−C(1)−O(1)	179.97(2)	179.92(22)
Cr−C(2)−O(2)	179.39(2)	179.05(21)
Cr−C(3)−O(3)	179.430(19)	179.37(15)
Cr−C(4)−O(4)	179.225(19)	179.20(14)
C(1)−Cr-C(2)	179.521(9)	179.56(10)
C(3)−Cr-C(4^i)	179.194(7)	179.10(6)
	$Fe(CO)_5$	
Fe−C(1)	1.8131(3)	1.804(2)
Fe−C(2)	1.8187(3)	1.811(2)
Fe−C(3)	1.8098(5)	1.801(3)
C(1)−O(1)	1.1451(5)	1.136(2)
C(2)−O(2)	1.1387(5)	1.117(2)
C(3)−O(3)	1.1444(9)	1.128(4)
Fe−C(1)−O(1)	179.70(3)	179.4(2)
Fe−C(2)−O(2)	179.54(3)	179.43(15)
Fe−C(3)−O(3)	180	180
C(2)−Fe-C(2^i)	178.818(17)	178.94(10)
C(1)−Fe-C(3)	121.439(9)	121.11(5)
C(1)−Fe-C(1^i)	117.122(18)	117.78(10)
C(1)−Fe-C(2^i)	90.395(11)	90.39(7)
C(2)−Fe-C(3)	89.409(9)	89.47(5)
	$Ni(CO)_4$	
Ni−C(1)	1.8283(7)	1.819(3)
Ni−C(2)	1.8249(4)	1.815(2)
C(1)−O(1)	1.1392(11)	1.125(3)
C(2)−O(2)	1.1376(7)	1.128(2)
Ni−C(1)−O(1)	180	180
Ni−C(2)−O(2)	179.42(3)	179.66(15)
C(1)−Ni-C(2)	109.209(9)	109.29(6)
C(2)−Ni-C(2^i)	109.732(9)	109.65(6)

[a] From ref 8 for $Cr(CO)_6$ and from ref 9 for $Fe(CO)_5$ and $Ni(CO)_4$.

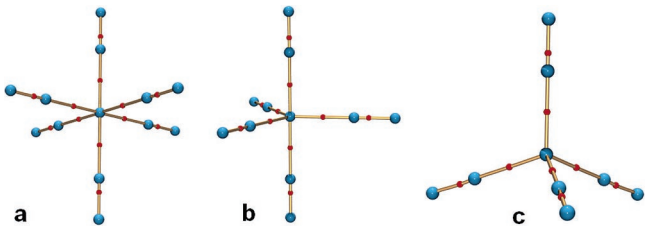

Figure 4. Experimental molecular graphs for (a) $Cr(CO)_6$, (b) $Fe(CO)_5$, and (c) $Ni(CO)_4$. Blue spheres indicate the atomic positions and red spheres the (3,−1) bond critical points in ρ. The viewpoints are the same as in Figures 1−3.

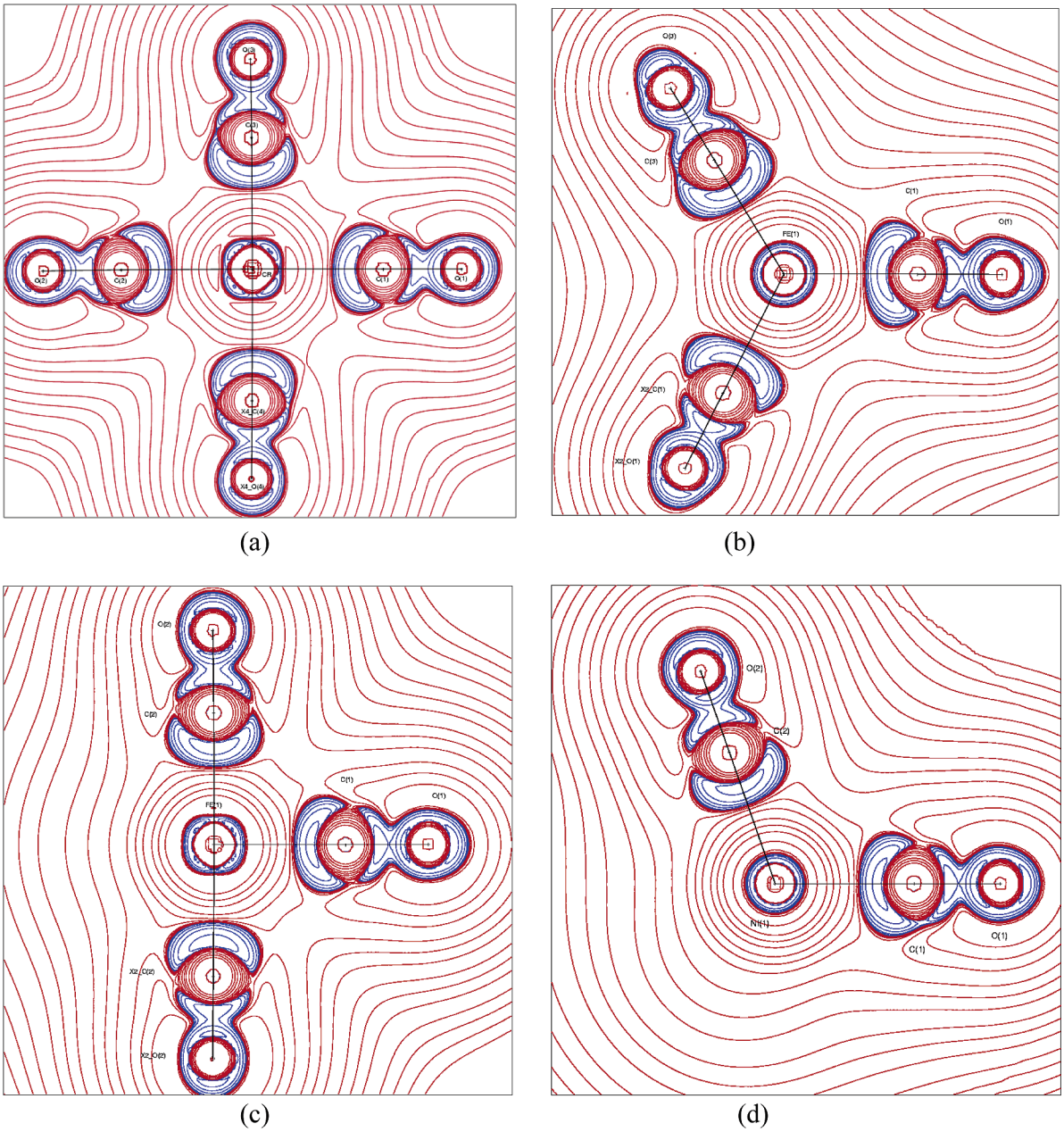

Figure 5. Plots of the experimental Laplacian $L \equiv -\nabla^2\rho(\mathbf{r})$, with positive contors drawn in blue and negative contors in red: (a) in the Cr−C1−C2−C3 plane of **1**, (b) in the Fe−C1−C3 plane of **2**, (c) in the Fe−C1−C2 plane of **2**, and (d) in the Ni−C1−C2 plane of **3**. Contours are drawn at -1.0×10^{-3}, $\pm 2.0 \times 10^{n}$, $\pm 4 \times 10^{n}$, $\pm 8 \times 10^{n}$ ($n = -3, -2, -1, 0, +1, +2$) e Å^{-5}.

The M−C interatomic surface lies in a region of charge depletion of the metal atom, resulting in a positive value for $\nabla^2\rho(\mathbf{r})$. This is clearly seen in Figure 5, which shows a plot of the Laplacian function $L \equiv -\nabla^2\rho(\mathbf{r})$ of molecules **1**−**3** through selected planes. The combination of bcp indices for the M−C bonds in Tables 3−5, i.e. small $\rho(\mathbf{r})$, positive $\nabla^2\rho(\mathbf{r})$, and negative $E(\mathbf{r}_b) = G(\mathbf{r}_b) - V(\mathbf{r}_b)$, are quite characteristic of bonding to a low-valent transition metal, and taking into account also the relatively large delocalization indices δ(M,C) seen in these systems,[14,15] it is clear that a description of such bonds as having closed-shell or ionic character is inappropriate. We prefer to describe these interactions as typical covalent interactions for transition metals. However, the mapping of the topological characteristics of bonds involving transition metals onto traditional chemical concepts such as covalent or ionic remains a point of some contention in the literature. For instance, Gervasio et al.[47] have recently applied Espinosa's proposed classification[48] of atomic interactions (closed-shell, transit, and shared-shell) to compounds containing transition-metal−metal bonds and concluded that the metal−metal bond in $Mn_2(CO)_{10}$ has the same nature as that in bulk metals. This viewpoint was disputed by Ponenc et al.[49] on the basis of a study of the domain-averaged Fermi holes. It was concluded that two main interactions provide the chemical bond between the two $Mn(CO)_5$ fragments, a homopolar Mn−Mn bond and 1,3-Mn···C interactions—a viewpoint also reached by Macchi and Sironi[14] from consideration of their delocalization indices.

While both models A and B provide an overall excellent fit with the theoretical values obtained for $Cr(CO)_6$, there are some small discrepancies. A comparison of the experimental and theoretical positions of the bond critical points reveals that for all M−C bonds, the interatomic surface is shifted slightly toward the metal atom in the theoretical wave function density. There is no similar trend in the position of the bcp for the C−O bonds, but the experimental values of $\rho(\mathbf{r})$ are consistently larger than the theoretical values, and the magnitudes of $\nabla^2\rho(\mathbf{r})$ are

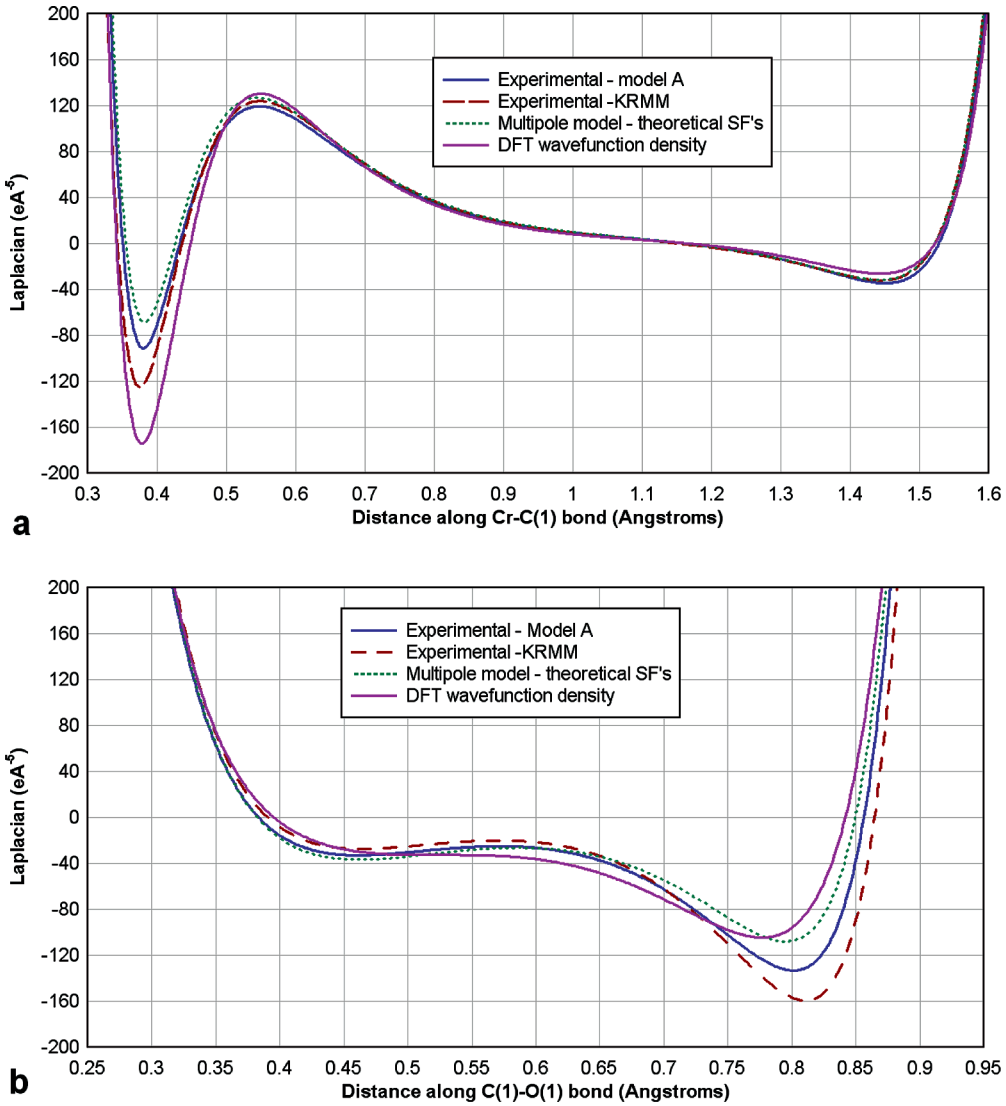

Figure 6. Profile of $\nabla^2\rho(\mathbf{r})$ in the valence region along (a) the Cr−C(1) bond and (b) the C(1)−O(1) bond in **1**.

consistently smaller. Moreover, the Cr−C bonds have consistently smaller $\rho(\mathbf{r})$ in the experimental data, while for the Fe−C and Ni−C bonds this trend is reversed. The root of the differing values for $\nabla^2\rho(\mathbf{r})$ lies in the magnitudes of λ_3, which are consistently larger in the theoretical data for the C−O bcp's and generally smaller in the theoretical data for the M−C bcp's. Similar features of polar covalent bonds were first noted by Gatti et al.[50] and have been remarked on subsequently.[51] They are usually attributed to limitations in the flexibility of the single-exponential Slater-type radial functions used,[40,51a,52] but in a word of caution, we note that Coppens and co-workers[53] find that the use of Slater-type functions for the wave function leads to better fits between experiment and theory.

It is informative to examine the behavior of the Laplacian function along the whole internuclear vector with the various models. Figure 6 show typical plots of $\nabla^2\rho(\mathbf{r})$, along the Cr−C(1) and C(1)−O(1) bond vectors, which closely resemble the corresponding to theoretical plots of Macchi and Sironi.[14] In the region of the bcp's, all models agree very well. The bcp for the Cr−C bond is in a region where $\nabla^2\rho(\mathbf{r})$ is slowly varying, so this function is insensitive to minor variations in the position of the bcp. On the other hand, the bcp for the C−O bond lies in a region where $\nabla^2\rho(\mathbf{r})$ is close to zero and sharply varying, and this accounts for the well-established difficulty of obtaining good agreement between theory and experiment for C−O bonds. The most obvious disagreements between all the multipole based models and the wave function densities are in the regions of charge concentrations on the Cr and O atoms. The Laplacian in the valence shell charge concentration (VSCC) on the Cr atom is sharper in the wave function density, and here the KRMM provides a significantly better fit than model A. Conversely in the region of the VSCC of the O atom, the wave function Laplacian is shallower than all the multipole based models, and the KRMM provides a worse agreement with theory than model A. A quantitative measure of the total fit along the bond vectors is given by R_{par} where

$$R_{\mathrm{par}} = \Sigma(|f_{\mathrm{model}} - f_{\mathrm{theor}}|)/\Sigma(|f_{\mathrm{theor}}|)$$

and f_{theor} is the theoretical value of the function—in this case $\nabla^2\rho(\mathbf{r})$—and f_{model} is the function value provided by the model at that point. A total of 800 points were used, but the core regions closer than ∼0.2 Å to the nuclei were not included in the summation. These R_{par} values (Supporting Information Table 3) indicate that for all independent Cr−C and C−O bonds, the KRMM model B provides a poorer fit to the theoretical values than model A, while model C generally gives the best fit. Clearly a more extensive examination of the applicability of the KRMM[34] for transition-metal compounds is needed. Although static structure factors were also computed for the $Fe(CO)_5$ and

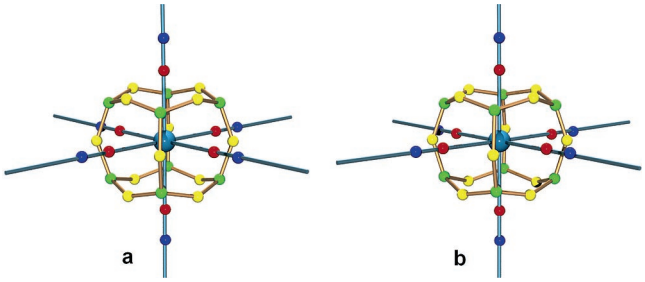

Figure 7. Atomic graph of the Cr atom in **1** (a − theoretical, b − experimental) showing the critical points in $L(\mathbf{r}) \equiv -\nabla^2\rho(\mathbf{r})$ in the VSCC. Color coding is (3,−3) green, (3,−1) yellow, (3,+1) red, (3,+3) blue (in VSCD).

$Ni(CO)_4$ structures, initial refinements with XD using these theoretical structure factors showed that the κ' parameters for the metal atoms did not converge well. This problem was especially severe for $Ni(CO)_4$, where refinement of κ' for Ni was unstable. For this reason, the KRMM for these structures were not further examined.

Atomic Graphs. While the topology of the density $\rho(\mathbf{r})$ is most commonly analyzed, there is a great deal of chemical information also in the topology of the Laplacian of ρ, $\nabla^2\rho(\mathbf{r})$. For instance, it is through analysis of $\nabla^2\rho(\mathbf{r})$ that the AIM theory provides a physical basis for the well-known VSEPR rules.[10] In general, the complete topology of $\nabla^2\rho(\mathbf{r})$ for an atom is complex, and rarely analyzed,[54] but one facet which is of interest is the atomic graph,[10] i.e. the set of critical points in $L(\mathbf{r}) \equiv -\nabla^2\rho(\mathbf{r})$ in the VSCC of the bonded atoms. For the first row transition metals this is the third shell, sometimes referred to[13] as the inner valence shell, *i*-VSCC. The atomic graph provides an easily visualized and concise representation of the distortion in the valence density of that atom,[55] which arises from chemical bonding. In a recent study, Bader and co-workers[56] show that the atomic graph of a transition-metal atom is a sensitive mirror of its coordination geometry.

Figure 7 shows the atomic graph of the Cr atom in $Cr(CO)_6$, determined from both the theoretical and experimental densities, and Table 7 lists the values of $\rho(\mathbf{r})$, $L(\mathbf{r})$, and the distance **r** from the nucleus for the critical points. This graph is the characteristic cuboidal [8,12,6] set for an octahedrally coordinated transition-metal atom[13−15] reported in several experimental charge density studies.[20,57] Eight charge concentrations, the (3,−3) critical points, are arranged in a cube, with 12 (3,−1) saddle points along all edges and six (3,+1) charge depletions in each face. The metal charge concentrations maximally avoid the ligand charge concentrations, consistent with the simple ligand-field approach. The (3,+1) charge depletions in the VSCC face the directions of the carbonyl ligands, and the (3,+3) critical points in the valence shell charge depletion (VSCD) lie in the same directions and further from the nucleus. The experimentally obtained atomic graph for the Cr atom in $Cr(CO)_6$ is thus essentially identical to the theoretical one. The experimental Laplacian isosurface plot shown in Figure 8a may be compared with similar theoretical plots from refs 14 and 15. As mentioned above, this atomic graph provides a clear illustration of the "lock and key" view of the chemical bonding of the carbonyl ligands to the metal atom. The large charge concentrations on the C atoms match the charge depletions on the metal.

In the case of $Fe(CO)_5$, we find the experimental atomic graph of the Fe atom to be dependent on the multipole model used to describe the metal atom. The theoretical atomic graph,[13,15] shown in Figure 9a, is of the [6,9,5] form, where the six charge concentrations define a trigonal prism. In the crystal structure of **2**, the Fe atom resides on a site of crystallographic C_2 symmetry. If the multipole populations are merely restricted by this site symmetry, the resultant atomic graph (Figure 9b) is of the cuboidal [8,12,6] form seen for the Cr atom in **1**. It does not comply with the molecular D_{3h} symmetry; in fact it does not display 3-fold symmetry along the axial direction. Under D_{3h} site-symmetry, the only allowed nonzero multipole populations for the Fe atom are P_{00}, P_{20}, P_{33-}, and P_{40}. When this restriction is applied, an atomic graph of the form [6,9,5] (Figure 9d) is obtained. This resembles the theoretical graph, but with the small difference that the three (3,+3) charge depletions in the VSCD in the equatorial plane lie along the same radial

TABLE 7. Critical Points in the Laplacian of ρ in the VSCC of the Metal Atoms

molecule	CP type		$\rho(\mathbf{r})$ (eÅ^{-3})	$L(\mathbf{r}) \equiv -\nabla^2\rho(\mathbf{r})$ (eÅ^{-5})	distance **r** (Å)
$Cr(CO)_6$	(3,−3)		16.628	573.294	0.355
			15.873	*605.123*	*0.359*
	(3,−1)		15.515	439.851	0.360
			14.949	*489.764*	*0.363*
	(3,+1)		12.234	93.845	0.380
			12.219	*171.758*	*0.378*
	(3,+3)		4.609	−118.385	0.549
			4.446	*−130.967*	*0.549*
$Fe(CO)_5$	(3,−3)		23.708	928.029	0.322
			24.439	*1032.359*	*0.323*
	(3,−1)	− ax	23.684	925.756	0.322
			23.825	962.241	0.325
		− eq	22.286	634.519	0.328
			22.246	*658.733*	*0.331*
	(3,+1)	− ax	17.656	213.829	0.341
			17.658	193.750	0.345
		− eq	22.238	630.085	0.328
			20.970	*521.538*	*0.335*
	(3,+3)	− ax	6.628	−202.332	0.498
			6.807	*−251.190*	*0.491*
		− eq	6.644	−162.736	0.524
			6.821	*−206.346*	*0.514*
$Ni(CO)_4$	(3,−3)		34.11	1316.5	0.294
			34.55	*1385.4*	*0.297*
	(3,−1)		34.18	1281.1	0.294
			34.25	*1366.4*	*0.298*
	(3,+1)		33.76	1256.3	0.294
			32.03	*1055.0*	*0.303*
	(3,+3)		9.56	−264.6	0.479
			9.71	*−333.4*	*0.475*

[a] For each entry, the first line is the averaged experimental value, and the second line is the theoretical value.

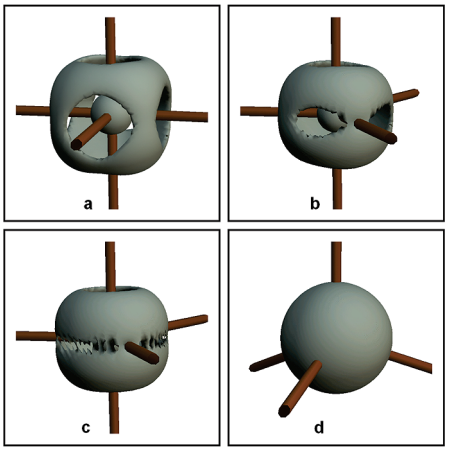

Figure 8. Isosurface plots of the experimental Laplacian $L(\mathbf{r}) \equiv -\nabla^2\rho(\mathbf{r})$ around the metal atoms in (a) $Cr(CO)_6$ (b) $Fe(CO)_5$ C_2 model, (c) $Fe(CO)_5$ D_{3h} model, and (d) $Ni(CO)_4$. The isosurface levels are 350, 630, 630, and 800 e Å^{-5}, respectively.

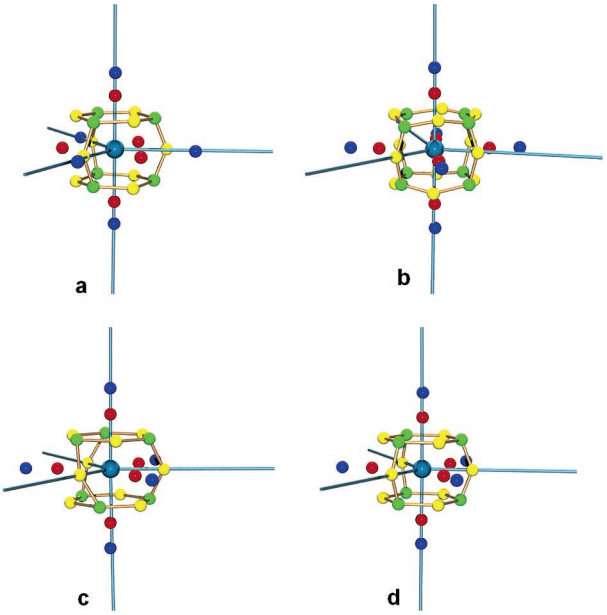

Figure 9. Atomic graphs of the Fe atom in **2** (a − theoretical, b−d experimental) showing the critical points in $L(\mathbf{r}) \equiv -\nabla^2\rho(\mathbf{r})$ in the VSCC. Color coding is (3,−3) green, (3,−1) yellow, (3,+1) red, (3,+3) blue (in VSCD). The multipole populations of the Fe atom are restricted to C_2 symmetry for (b), to D_3 symmetry for (c), and D_{3h} symmetry for (d).

direction as the (3,+1) depletions, rather than opposed to the equatorial ligands as in the theoretical atomic graph. An atomic graph of the [6,9,5] form, shown in Figure 9c, also results when the multipole populations are restricted to D_3 site-symmetry (the multipole P_{43} is now also allowed). In this case the charge concentrations define a *skewed* trigonal prism. The multipole populations for these three models are given in Supporting Information Table S2. This observed model dependency cannot be attributed solely to the small deviations from idealized D_{3h} symmetry in the experimental structure. Gas-phase DFT calculations on $Fe(CO)_5$ in the experimentally observed C_2 geometry gave an atomic graph essentially identical to that for strict D_{3h} geometry. A theoretical topological study[58] on the trigonal bipyramidal (tbp) complex VF_5 shows a very different atomic graph for the V atom, with the [5,9,6] form in which there are five ligand opposed charge concentrations arranged in a tbp. This sensitivity of the atomic graph of the transition metal to the ligand coordination sphere relates to the differing interactions of the metal *d*-orbitals with π-donor ligands in VF_5, compared with π-acid ligands in $Fe(CO)_5$. There have been very few *experimental* charge-density topological studies on tbp transition-metal compounds—the only one of which we are aware is $Co_2(CO)_6(AsPh_3)_2$.[59] The atomic graph of one of the Co atoms has the form [6,9,5] with C_3 symmetry[60] and is quite similar to that of the D_3 restricted model for $Fe(CO)_5$.

For $Ni(CO)_4$ the situation is more difficult. The third quantum shell of Ni is formally complete with the d^{10} configuration.[61] The VSCC is nearly spherically symmetric, with the values for $\rho(\mathbf{r})$ and $L(\mathbf{r})$ for the (3,−3), (3,−1), and (3,+1) cp's being very close in magnitude (see Table 7). The theoretical atomic graph[13,15] is basis-set dependent, while maintaining overall tetrahedral symmetry. The standard tetrahedral [4,6,4] atomic graph, such as is found for the C atom in methane,[10] is observed when using a limited basis,[13] but it becomes more complicated with a more extensive basis set.[13,15] Each of the six (3,−1) saddle-point cp's bifurcates into a new (3,−3) cp and two associated (3,−1) cp's, which are very close together and have very similar densities. We obtain a theoretical atomic graph

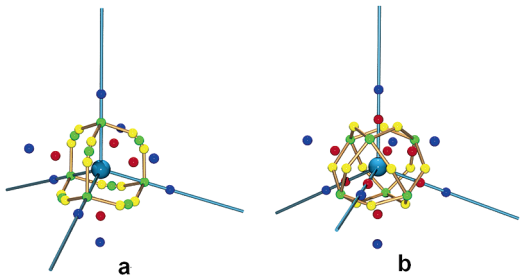

Figure 10. Atomic graph of the Ni atom in **3** (a − theoretical, b − experimental) showing the critical points in $L(\mathbf{r}) \equiv -\nabla^2\rho(\mathbf{r})$ in the VSCC. Color coding is (3,−3) green, (3,−1) yellow, (3,+1) red, (3,+3) blue (in VSCD).

(Figure 10a) which is very similar to that reported previously,[13,15] except that an extra set of (3,+3) cp's in the VSCD were observed. These lie in the same radial direction as the set of (3,+1) cp's. The experimental study reproduces the nearly spherical density in the VSCC, as is clearly visible from Figures 5 and 8. This nearly spherical density of the Ni atom contrasts with that found in octahedral or square-planar Ni(II) coordination complexes,[62] which show very clearly defined charge concentrations in the Laplacian maps. On the other hand, the Ni atom in the related zerovalent compound $Ni(COD)_2$ also displays[63] a nonspherical charge distribution. The atomic graph of the Ni atom obtained from multipole populations is quite model dependent and differs substantially from the gas-phase theoretical one. For both the C_3 and T_d models, the graph has the octahedral [6,12,8] topology, with six charge concentrations lying on the edges of the coordination tetrahedron, one set of four ligands opposed charge depletions, and another set of four charge depletions aligned along the Ni−C vectors. The positions of the (3,−1) saddle points differ between the C_3 and T_d models and give rise to visually distinct graphs. The graph from the T_d model is shown in Figure 10b. Despite the differences in the topology of the atomic graphs, the radial positions and magnitudes of $\rho(\mathbf{r})$ and $L(\mathbf{r})$ given in Table 7 compare reasonably well with the theoretically derived values.

The difficulties in recovering the theoretical (gas phase) atomic graphs from the experimental data for compounds **2** and **3** led us to investigate possible causes. Systematic errors in the experimental data introduced by the data processing methodology, in particular the SADABS "absorption" correction program,[22a] were one potential cause. To eliminate this possibility, the raw data were reprocessed as described in the Experimental Section. The atomic graphs obtained for **2** using the multipole models described above were essentially identical, eliminating this as a cause. Deficiencies in the multipole methodology or in the radial functions used[40,50−52] were also examined. Multipole models were refined against theoretical static structure factors obtained from periodic DFT(B3LYP) calculations on **2** and **3** (based on the experimental crystal structure). For compound **2**, the same C_2 restricted multipole model described above gave an atomic graph identical to that shown in Figure 9d, i.e. virtually the same as the gas-phase theoretical [6,9,5] tbp graph.[13,15] In contrast, for **3** we are unable to reproduce the gas-phase theoretical atomic graph from any multipole model. The derived atomic graphs have the same [6,-12,8] topology as obtained from the experimental multipole models. It seems unlikely that this is a crystal effect. The sensitivity of the multipole refinement to random errors in the data was also tested by refinement against sets of static structure factors with random noise introduced into F_{hkl} up to maximum levels of ±1, ±5, and ±10%. The refinements for compound **2** are not substantially affected by the random errors, but for **3**

TABLE 8. Atomic Charges

atom	$q(P_v)^{a,c}$	$q(\Omega)^{a,d,e}$	$q(\Omega)^{a,d,f}$	$q(\mathrm{Orb})^{b,g}$	$q(\Omega)^{b,d}$
Cr(1)	0.90(4)	1.062	1.031	−0.748	1.160
C(1)	−0.02(4)	1.013	1.027	0.383	0.934
C(2)	0.06(5)	1.001	0.997	0.395	0.938
C(3)	−0.10(3)	1.022	1.035	0.386	0.911
C(4)	−0.08(3)	0.988	0.981	0.395	0.906
O(1)	−0.27(4)	−1.336	−1.180	−0.268	−1.119
O(2)	−0.05(5)	−1.020	−1.082	−0.266	−1.119
O(3)	−0.07(3)	−1.214	−1.213	−0.265	−1.121
O(4)	−0.06(3)	−1.148	−1.193	−0.267	−1.121
sum[h]	0.00	0.018	0.013	0.000	0.056
Fe(1)	0.18(3)	0.835		1.301	0.728
C(1)	−0.20(3)	0.952		−0.166	0.945
C(2)	−0.18(3)	1.025		−0.031	0.997
C(3)	−0.32(4)	0.856		−0.166	0.945
O(1)	0.21(2)	−1.081		−0.172	−1.116
O(2)	0.21(2)	−1.113		−0.171	−1.107
O(3)	0.07(4)	−1.244		−0.113	−1.116
sum[h]	0.00	0.011		0.001	0.000
Ni(1)	0.15(8)	0.675		0.695	0.515
C(1)	−0.32(6)	0.903		−0.096	0.996
C(2)	−0.22(5)	1.018		−0.096	0.996
O(1)	0.10(5)	−1.243		−0.078	−1.125
O(2)	0.24(4)	−1.126		−0.078	−1.125
sum[h]	−0.003	0.012		−0.001	−0.001

[a] From experimental study. [b] From DFT calculations. [c] From monopole populations. [d] AIM charges from atomic basin integration. [e] Model A for $Cr(CO)_6$. [f] Model B (KRMM) for $Cr(CO)_6$. [g] From Mulliken population analysis. [h] Charges are summed over the complete molecule, including symmetry related atoms.

the main effect are shifts in the positions of the (3,−1) saddle points, which are detectable for the C_3 model even for the ±1% random error data (see Supporting Information Figure S31). The C_3 model, with more refinable multipole parameters, is more sensitive to random error than the T_d model. This result indicates that, in unfavorable cases at least, it may be difficult to obtain accurate atomic graphs from experimental data. Remaining potential causes of the discrepancy between experiment and theory include unrecognized systematic errors in the data or incomplete thermal motion deconvolution.

Atomic Charges. Atomic charges describe the redistribution of electrons which accompany the formation of chemical bonds, and while the concept is extremely useful in chemical rationalization, the measurement of atomic charges is fraught with problems.[64] The AIM methodology offers a less arbitrary way of determining atomic charges, through integration of the electron population within the atomic basins. These "Bader" integrated charges are computationally expensive, due to the difficulty of determining the interatomic surface,[43,44,65] and can be quite sensitive to the models used to construct the density. They have often been criticized for being too large and not in line with "chemical intuition",[66a] but these criticisms have been addressed by Bader.[66b] Bultinck et al.[67] have proposed a new approximate method for the rapid calculation of these quantities.

The atomic charges as determined by several methods are given in Table 8. To examine any model dependency for the atomic basin integrated charges, both model A (free kappa refinement) and model B (KRMM) for $Cr(CO)_6$ were investigated. Although the individual charges vary somewhat, especially for the O atoms, the mean charges for O and C atoms (−1.180 and 1.006 for model A and −1.179 and 1.009 for model B, respectively) are essentially identical and are in reasonable agreement with the theoretical charges.[14,15] It should be noted that, in the integrations, the atomic basins in the gas phase theoretical calculations were arbitrarily truncated at 9 au, while those in the crystal phase terminate through the intermolecular interactions with other molecules, so the two are not strictly comparable. Nevertheless the agreement is surprisingly good, with the experimental charges on the Cr atom being slightly less positive and the charges on the C atoms slightly more positive than the theoretical charges. The agreement between experiment and theory is also quite reasonable for $Fe(CO)_5$ and $Ni(CO)_4$, though the experimental charge on the metal for these is slightly greater. The average transfer of charge from the metal to each carbonyl ligand follows the order Cr > Fe ∼ Ni. The theoretical Bader charges[15] follow the order Cr > Fe > Ni, which is quite consistent with simple ideas of back-donation, as the mean ν(CO) stretching frequencies are respectively 2017, 2044, and 2077 cm^{-1}.

TABLE 9. Unabridged Atomic Quadrupole Moments $Q(\Omega)$

atom	Q_{xx}	Q_{yy}	Q_{zz}	Q_{xy}	Q_{xz}	Q_{yz}	$\lvert Q\rvert^b$
C[a]	−2.759	−2.893	−2.893	0	0	0	0.164
	−2.064	−2.964	−2.964	0	0	0	0.900
O[a]	−4.700	−4.816	−4.816	0	0	0	0.115
	−4.600	−4.774	−4.774	0	0	0	0.175
			$Cr(CO)_6$				
C1	−1.939	−2.734	−2.762	0.002	0	0	0.809
C2	−1.956	−2.643	−2.760	−0.027	0.001	0.002	0.752
C3	−1.958	−2.597	−2.737	−0.037	0.007	−0.003	0.719
C4	−1.923	−2.730	−2.730	0.036	−0.012	−0.023	0.806
O1	−4.723	−4.819	−4.710	−0.061	0	0	0.102
O2	−4.497	−4.247	−4.142	0.002	0	0	0.316
O3	−4.498	−4.571	−4.550	0.019	0.026	−0.019	0.065
O4	−4.451	−4.532	−4.539	0.012	−0.051	−0.047	0.085
			$Fe(CO)_5$				
C1	−3.390	−2.994	−1.949	−0.036	−0.018	−0.004	1.289
C2	−2.913	−2.957	−1.922	−0.001	−0.007	0.002	1.013
C3	−3.574	−3.073	−1.937	−0.076	−0.004	−0.003	1.453
O1	−4.626	−4.693	−4.639	−0.028	−0.008	0.003	0.062
O2	−4.776	−4.801	−4.625	−0.022	0	0.007	0.164
O3	−4.749	−4.897	−4.788	0.041	0	0	0.132
			$Ni(CO)_4$				
C1	−3.249	−3.243	−2.047	0.002	0	0	1.199
C2	−3.122	−3.099	−2.049	0	−0.008	0.006	1.061
O1	−4.816	−4.816	−4.663	0	0	0	0.152
O2	−4.696	−4.684	−4.671	−0.004	0.004	0.006	0.022

[a] Theoretical values for the carbonyl group: the first line is for free CO molecule DFT/B3LYP 6-311++G(2d), the second line is for $Cr(CO)_6$ O_h geometry optimized DFT/B3LYP. Other values are experimentally derived from the atomic basin integrations. The C−O vectors define the local x axis, except for $Fe(CO)_5$ and $Ni(CO)_4$ where they define the z axis. [b] $|Q| = (2/3[Q_{xx}^2 + Q_{xx}^2 + Q_{xx}^2])^{1/2}$ where Q_{xx}, etc. are the components of the *traceless* quadrupole moment.

Atomic Quadrupole Moments. The atomic quadrupole and higher moments provide a concise description of the atomic charge density and are routinely available from X-ray diffraction data.[69] Of particular interest here are the quadrupole moments of the C and O atoms. As suggested by Cortés-Guzmán and Bader,[15] these may provide a direct measurement of the relative degrees of σ-donation and π-back-donation upon complexation and hence provide direct evidence for the commonly accepted back-bonding model for CO binding. The quadrupole moment of an axially symmetric ligand like CO indicates the accumulation of density along the axis (||) as opposed to density in a torus about this axis (⊥), which may be associated respectively with the σ- and π-densities. Table 9 shows the experimentally derived unabridged[70] quadrupole moments from the atomic basin integrations and those calculated from the wave functions. The magnitudes of the moments of the C atom perpendicular to the reference axis (either x or z—see Table 9) increase significantly when the CO ligand is coordinated to the metal atom, while that for the O atoms is much less affected. The agreement with theory for $Cr(CO)_6$ is very good. This is consistent[15] with a

TABLE 10. *d*-orbital Populations[a]

d-orbital	**1**[b]	**1**[c]	**2**	**3**
z^2	0.917(9)	0.410	0.588(20)	1.593(8)
	0.949	*0.306*	*0.618*	*1.701*
xz	1.122(8)	1.101	1.268(12)	1.567(5)
	1.169	*1.135*	*1.425*	*1.555*
yz	0.362(8)	1.031	1.268(12)	1.567(5)
	0.277	*1.162*	*1.425*	*1.555*
x^2-y^2	0.566(8)	0.415	1.347(15)	1.593(7)
	0.482	*0.252*	*1.181*	*1.701*
xy	1.134(8)	1.144	1.347(15)	1.567(6)
	1.172	*1.194*	*1.181*	*1.555*
total	4.101	4.101	5.818	7.887
	4.049	*4.049*	*5.830*	*8.067*

[a] The top line is experimental values, and the second line is from multipole refinements against theoretical static structure factors. [b] Original global coordinate system. [c] Populations after rotation of coordinate system.[71]

preferential accumulation of charge in the π-orbitals compared with the σ-orbitals, indicating significant π-back-donation into the π^* orbital of CO, which is heavily localized on the C atom. However, some caution should be exercised in interpreting moments from an AIM analysis, since they depend both on the charge distribution inside the atomic basin and on its shape and size. The atomic volume of the C atom in CO contracts from 118 to 77 au when complexed in $Cr(CO)_6$ (while the atomic volume of the O atom is essentially unchanged), and the main effect is to reduce the Q_{xx} component.

***d*-Orbital Populations.** Table 10 shows the *d*-orbital populations calculated from the multipole populations by the method of Coppens et al.[17a] The orbital populations so derived are dependent on the local coordinate system which is used to describe the multipoles. For $Cr(CO)_6$ the crystallographic symmetry requires a local coordinate system which is not aligned with the octahedral molecular axes. As described by Sabino and Coppens,[71] the local coordinate system may be rotated to bring it into coincidence. The new populations for $Cr(CO)_6$ in this rotated frame are also shown in Table 10. As expected from a simple ligand field approach, the e_g set is depopulated compared with the t_{2g}, with a population ratio 1:3.97, which is close to the value originally obtained by Rees and Mitschler.[8] Under the D_{3h} symmetry of $Fe(CO)_5$, the *d*-orbitals transform as a_1' (z^2), e'' (*xz*, *yz*), and e' ($x^2 - y^2$, *xy*). The e'' set are only involved in π-interactions with the set of equatorial CO ligands. They are less destabilized than the e' set which are involved in both σ- and π-interactions with these CO ligands and in π-interactions with the axial carbonyls. The a_1' set is only involved in σ-bonding with the axial carbonyls and is the most strongly destabilized. The experimental populations in Table 10 show that the e' is slightly more populated than the e'', though the populations from refinement against theoretical structure factors show the expected ligand field ordering. For $Ni(CO)_4$, the virtually spherical density of the valence shell results in almost identical *d*-orbital populations. The overall populations obtained for **1** and **2** agree remarkably well with the theoretical *d*-orbital populations reported by Cortés-Guzmán and Bader[15] (4.1 and 5.8e, respectively), but that for **3** differs significantly from theory (9.09e). The reason lies in the multipole model used for **3**, which assumed the $4s^2 3d^n$ valence configuration. A refinement using a $3d^n$ valence model gave a *d*-orbital population of 8.36 e, but since it resulted in a significantly worse fit ($R_F = 1.26$, GOF = 1.98, compared with $R_F = 1.16$, GOF = 1.88), it was not considered worth pursuing.

Conclusions

This paper reports experimental high-resolution X-ray studies on $Cr(CO)_6$ (**1**), $Fe(CO)_5$ (**2**), and $Ni(CO)_4$ (**3**), which provide to date the most accurate solid-state structures of these important molecules. The topological properties at the bond critical points in the charge densities, as obtained from the standard multipole modeling, are in excellent agreement with theory and are typical of covalent interactions involving transition metals. The expansion-contraction parameters κ' for the deformation valence radial functions have proven to be difficult parameters to converge. It is for this reason that the KRMM has been proposed, where the κ' parameters are fixed at values obtained from the refinements against theoretical structure factors. Such a model was tested for $Cr(CO)_6$ but gave a worse agreement than with freely refined κ' parameters. The main difference is that the κ' parameter for the O atom refines to give a much more diffuse radial function in the freely refined model.

The atomic graphs for the metal atoms in compounds **2** and **3** obtained from multipole refinements are quite model dependent, and those for **3** are also sensitive to random errors in the data. This suggests that, in unfavorable cases at least, accurate atomic graphs may be difficult to obtain from experimental data. The structures considered here are all centrosymmetric, and this problem could be more severe for noncentrosymmetric structures, which suffer additional ambiguity from phase uncertainties.

Acknowledgment. We thank the EPSRC for Grant GR/M91433 toward the purchase of a KappaCCD diffractometer. The New Zealand Foundation for Research, Science & Technology is thanked for financial (PDRA) support for C.E. We especially thank Dr. Piero Macchi (Milano) for many helpful discussions and for the calculation of theoretical structure factors for **1** and Dr. Anatoliy Volkov for supplying the programs to transform the coordinate systems of atomic moments.

Supporting Information Available: Final refined parameters; observed and calculated structure factors in CIF format for the spherical atom and multipole refinements; Figures S1−S31 of final residual maps, experimental deformation maps, dynamic and static model deformation maps, and Laplacian maps; and tables of harmonic and anharmonic thermal parameters and multipole populations for three multipole models for $Fe(CO)_5$ and values of R_{par} comparing theoretical and model distributions of the Laplacian along the Cr−C and C−O bonds in $Cr(CO)_6$. This material is available free of charge via the Internet at http://pubs.acs.org.

References and Notes

(1) (a) Kirtley, S. W. In *Comprehensive Organometallic Chemistry*; Wilkinson, G., Stone, F. G. A., Abel, E. W., Eds.; Pergamon Press: Oxford, 1982; Chapter 26.1 (b) Shriver, D. F.; Whitmire, K. H. In *Comprehensive Organometallic Chemistry*; Wilkinson, G., Stone, F. G. A., Abel, E. W., Eds.; Pergamon Press: Oxford, 1982; Chapter 31.1. (c) Jolly, P. W. In *Comprehensive Organometallic Chemistry*; Wilkinson, G., Stone, F. G. A., Abel, E. W., Eds.; Pergamon Press: Oxford, 1982; Chapter 37.1 (d) Winter, M. J. In *Comprehensive Organometallic Chemistry II*; Wilkinson, G., Stone, F. G. A., Abel, E. W., Eds.; Pergamon Press: Oxford, 1995; Vol. 5, Chapter 3. (e) Whitmire, K. H. In *Comprehensive Organometallic Chemistry II*; Wilkinson, G., Stone, F. G. A., Abel, E. W., Eds.; Pergamon Press: Oxford, 1995; Vol. 7, Chapter 1. (f) Kubiack, C. P. In *Comprehensive Organometallic Chemistry II*; Wilkinson, G., Stone, F. G. A., Abel, E. W., Eds.; Pergamon Press: Oxford, 1995; Vol. 9, Chapter 1.

(2) Frenking, G.; Frölich, N. *Chem. Rev.* **2000**, *100*, 717, and references therein. (b) Frenking, G.; Wichmann, K.; Frölich, N.; Loschen, C.; Lein, M.; Frunzke, J.; Rayon, V. M. *Coord. Chem. Rev.* **2003**, *238*−*239*, 55.

(3) Baerends, A. J.; Ros, P. *Mol. Phys.* **1975**, *30*, 1735. (b) Elian, M.; Hoffmann, R. *Inorg. Chem.* **1975**, *14*, 1058. (c) Bauschlicher, C. W.; Bagus,

P. S. *J. Chem. Phys.* **1984**, *81*, 5889. (d) Lüthi, H. P.; Siegbahn, P. E. M.; Almlöf, J. *J. Phys. Chem.* **1985**, *89*, 2156. (e) Ziegler, T.; Tschinke, V.; Ursenbach, C. *J. Am. Chem. Soc.* **1987**, *109*, 1825. (f) Barnes, L. A.; Rosi, M.; Bauschlicher, C. W. *J. Chem. Phys*. **1991**, *94*, 2031. (g) Kunze, K. L.; Davidson, E. R. *J. Phys. Chem.* **1992**, *96*, 2129. (h) Davidson, E. R.; Kunze, K. L.; Machado, F. B. C.; Chakravorty, S. J. *Acc. Chem. Res.* **1993**, *26*, 628. (i) Davidson, E. R.; Machado, F. B. C. *J. Phys. Chem.* **1993**, *97*, 4397. (j) Barnes, L. A.; Liu, B.; Lindh, R. *J. Chem. Phys* **1993**, *98*, 3978. (k) Ehlers, A. W.; Frenking, G. *J. Am. Chem. Soc.* **1994**, *116*, 1514. (l) Delley, B.; Wrinn, M.; Lüthi, H. P. *J. Chem. Phys.* **1994**, *100*, 5785. (m) Persson, B. J.; Roos, B. O.; Pierloot, K. *J. Chem. Phys.* **1994**, *101*, 6810. (n) Persson, B. J.; Taylor, P. R. *Theor. Chem. Acta* **2003**, *110*, 211. (m) Cioslowski, J.; Hay, R. F.; Ritchie, J. P. *J. Phys. Chem.* **1990**, *94*, 148. (n) Radius, U.; Bickelhaupt, F. M.; Ehlers, A. W.; Goldberg, N.; Hoffmann, R. *Inorg. Chem.* **1998**, *37*, 1080. (o) Fonseca Guerra, C.; Handgraaf, J.-W.; Baerends, E. J.; Bickelhaupt, F. M. *J. Comput. Chem.* **2004**, *25*, 189.

(4) Kohn, W.; Sham, L. *Phys. Rev. A* **1965**, *140*, 1133. (b) Parr, R. G.; Yang, W. *Density-Functional Theory of Atoms and Molecules*; Oxford University Press: New York, 1989. (c) Dreizler, R. M.; Gross, E. K. U. *Density Functional Theory, an Approach to the Quantum Many-Body Problem*; Springer-Verlag; Berlin, 1990. (d) *Electronic Density Functional Theory of Molecules, Clusters and Solids*; Ellis, D. E., Ed.; Kluwer Academic Publishers: Dordrecht, 1995. (e) *Recent Developments and Applications of Modern Density Functional Theory*; Seminario, J. M., Ed.; Elsevier: Amsterdam, 1996. (f) Te Veld, G.; Bickelhaupt, F. M.; Baerends, E. J.; Fonseca Guerra, C.; Van Gisbergen, S. J. A.; Snijders, J. G.; Ziegler, T. *J. Comput. Chem.* **2001**, *22*, 931.

(5) Hay, P. J.; Wadt, W. R. *J. Chem. Phys.* **1985**, *82*, 270.

(6) Whitaker, A.; Jeffrey, J. W. *Acta Crystallogr.* **1967**, *23*, 977. (b) Hanson, A. W. *Acta Crystallogr.* **1962**, *15*, 930. (c) Donahue, J.; Caron, A. *Acta Crystallogr.* **1964**, *17*, 663. (d) Ladell, J.; Post, B.; Fankuchen, I. *Acta Crystallogr.* **1952**, *5*, 795.

(7) Beagley, B.; Schmidling, D. *J. Mol. Struct.* **1974**, *22*, 466. (b) Hedberg, L.; Iijima, T.; Hedberg, K. *J. Chem. Phys.* **1979**, *70*, 3224. (c) Huang, J.; Hedberg, K.; Davis, H. B.; Pomeroy, R. K. *Inorg. Chem.* **1990**, *29*, 3923.

(8) Rees, B.; Mitschler, A. *J. Am. Chem. Soc.* **1976**, *98*, 7918.

(9) Braga, D.; Grepioni, F.; Orpen, A. G. *Organometallics* **1993**, *12*, 1481.

(10) Bader, R. F. W. *Atoms in Molecules: A Quantum Theory*; International Series of Monographs in Chemistry 2; Oxford University Press: Oxford, 1990. (b) Popelier, P. *Atoms in Molecules: An Introduction*; Prentice Hall: Harlow, 2000. (c) Gillespie, R. J.; Popelier, P. L. A. *Chemical Bonding and Molecular Geometry*; Oxford University Press: Oxford, 2001.

(11) Bader, R. F. W. *J. Phys. Chem. A* **1998**, *102*, 7314. (b) Matta, C. F.; Hernández-Trujillo, J.; Tang, T.-H.; Bader, R. F. W. *Chem. Eur. J.* **2003**, *9*, 1940.

(12) Haaland, A.; Shorokhov, D. J.; Tverdova, N. V. *Chem. Eur. J.* **2004**, *10*, 4416.

(13) MacDougall, P. J.; Hall, M. B. *Trans. Am. Cryst. Assoc.* **1990**, *26*, 105.

(14) Macchi, P.; Sironi, A. *Coord. Chem. Rev.* **2003**, *238*−*239*, 383 and references therein.

(15) Cortés-Guzmán, F.; Bader, R. F. W. *Coord. Chem. Rev.* **2005**. *249*, 633 and references therein.

(16) Coppens, P. *X-ray Charge Densities and Chemical Bonding*; Oxford Science Publications: Oxford, 1997. (b) Tsirelson, V. G.; Ozerov, R. P. *Electron Density and Bonding in Crystals*; Institute of Physics Publishing: Bristol, 1996. (c) Coppens, P. *Acta Crystallogr., Sect A* **1998**, *54*, 779−788. (d) Koritsanszky, T. S.; Coppens, P. *Chem. Rev.* **2001**, *101*, 1583.

(17) Holladay, A.; Leung, P. C. W.; Coppens, P. *Acta Crystallogr., Sect A* **1983**, *39*, 440. (b) Coppens, P. *Coord. Chem. Rev.* **1985**, *65*, 285.

(18) "Collect" data collection software, Nonius B.V., 1999. (b) Otwinowski, Z.; Minor, W. Processing of X-ray Diffraction Data Collected in Oscillation Mode. *Methods in Enzymology, Volume 276: Macromolecular Crystallography, Part A*; Carter, C. W., Jr., Sweet, R. M., Eds.; Academic Press: 1997; pp 307−326.

(19) Herbstein, F. H. *Acta Crystallogr. Sect., B* **2000**, *56*, 547.

(20) Farrugia, L. J.; Evans, C. *C. R. Acad. Sci., Ser. IIc: Chim*. **2005**, in press.

(21) Blessing, R. H. *DENZOX − Program for processing Denzo x files*; 1997. Farrugia, L. J.; Muir, K. W. modified for KappaCCD data, 2001.

(22) Sheldrick, G. *SADABS − A Bruker-Nonius program for area detector absorption and other corrections*, Version 2.10; 2003. (b) Farrugia, L. J.; Muir, K. W. *ABCYL − a program for correction of absorption and irradiation volume of cylindrical crystals from data collected on a KappaCCD diffractometer*; 2005. This program applies an analytical correction for the sample volume of irradiation, $v_{cor} = [1-\{\cos(\omega)\times[1-\cos(\kappa)]\times\sin(\alpha)\times\cos(\alpha) + \sin(\omega)\times\sin(\kappa)\times\sin(\alpha)\}^2]^{1/2}$ (where κ, ω are the kappa-goniostat angles and α is the kappa-support angle), and an absorption correction for a cylinder by Gaussian quadrature. The volume correction factor is an approximation based on the assumptions that (i) the cylinder length is effectively infinite compared with the diameter of the X-ray beam, (ii) the cylinder diameter is smaller than the beam width, and (iii) the beam is homogeneous. This factor varies quite substantially with the goniostat setting angles, and for those angle used in data collection, correction factors are typically in the range 1.0−0.6. An illustrative set of volume corrections for the low angle data set for compound **2** is shown in Supporting Information Figure S1. The calculated volume corrections were based on a beam diameter of 0.6 mm and are in reasonable agreement with the empirical scale factors applied by SADABS. The volume correction algorithm in ABCYL is based on that in the program KAPKOR − see Hellier, D. G.; Luger, P.; Buschmann, J. *Acta Crystallogr., Sect B* **1996**, *52*, 505.

(23) Blessing, R. H. *Acta Crystallogr., Sect A* **1995**, *51*, 33.

(24) Blessing, R. H. *J. Appl. Crystallogr.* **1997**, *30*, 421.

(25) Sheldrick, G. M. *SHELXL-97 a program for crystal structure refinement*, Release 97-2; University of Göttingen: Germany, 1997; .

(26) Tables 4.2.4.2, 4.2.6.8, and 6.1.1.4 from *International Tables for Crystallography, Volume C Mathematical, Physical and Chemical Tables*; Kluwer: Dordrecht, 1995.

(27) Farrugia, L. J. *J. Appl. Crystallogr.* **1997**, *30*, 565.

(28) Farrugia, L. J. *J. Appl. Crystallogr.* **1999**, *32*, 837.

(29) Coppens, P.; Leiserowitz, L.; Rabinovich, D. *Acta Crystallogr.* **1965**, *18*, 1035.

(30) Hansen, N. K.; Coppens, P. *Acta Crystallogr., Sect A* **1978**, *34*, 909.

(31) Koritsanszky, T.; Howard, S. T.; Richter, T.; Macchi, P.; Volkov, A.; Gatti, C.; Mallinson, P. R.; Farrugia, L. J.; Su, Z.; Hansen, N. K. *XD − A Computer program package for multipole refinement and topological analysis of charge densities from diffraction data*; 2003.

(32) Su, Z.; Coppens, P. *Acta Crystallogr., Sect A* **1998**, *54*, 646.

(33) Bunge, C. F.; Barrientos, J. A.; Bunge, A. V. *At. Data Nucl. Data Tables* **1993**, *53*, 113.

(34) Volkov, A.; Abramov, Y. A.; Coppens, P. *Acta Crystallogr., Sect A* **2001**, *57*, 272. (b) Abramov, Yu.; Volkov, A.; Coppens, P. *Chem. Phys. Lett.* **1999**, *311*, 81.

(35) Saunders, V. R.; Dovesi, R.; Roetti, C.; Orlando, R.; Zicovich-Wilson, C. M.; Harrison, N. M.; Doll, K.; Civalleri, B.; Bush, I. J.; D'Arco, Ph.; Llunell, M. *CRYSTAL03 program*; 2003.

(36) Mallinson, P. R.; Koritsanszky, T.; Elkaim, E.; Li, N.; Coppens, P. *Acta Crystallogr. Sect A* **1988**, *44*, 336.

(37) Hirshfeld, F. L. *Acta Crystallogr. Sect A* **1976**, *32*, 239.

(38) Smith, G. T.; Mallinson, P. R.; Frampton, C. S.; Farrugia, L. J.; Peacock, R. D.; Howard, J. A. K. *J. Am. Chem. Soc.* **1997**, *119*, 5028.

(39) Abramov, Y. A. *Acta Crystallogr., Sect A* **1997**, *53*, 264.

(40) Volkov, A.; Gatti, C.; Abramov, Yu.; Coppens, P. *Acta Crystallogr., Sect A* **2000**, *56*, 252.

(41) Flensburg, C.; Madsen, D. *Acta Crystallogr Sect A* **2000**, *56*, 24. (b) Aicken, F. M.; Popelier, P. L. A. *Can. J. Chem.* **2000** *78*, 415. (c) Bytheway, I.; Grimwood, D. J.; Jayatilaka, D. *Acta Crystallogr., Sect A* **2002**, *58*, 232.

(42) Guest, M. F.; Kendrick, J.; van Lenthe, J. H.; Sherwood, P. *GAMMES-UK*, version 6.3; 2002. The DFT module within GAMESS-UK was developed by Dr. P. Young under the auspices of EPSRC's Collaborative Computational Project No. 1 (CCP1, 1995−1997).

(43) Basis sets were obtained from the Extensible Computational Chemistry Environment Basis Set Database, Version 02/25/04, as developed and distributed by the Molec4ular Science Computing Facility, Environmental and Molecular Sciences Laboratory which is part of the Pacific Northwest Laboratory, P.O. Box 999, Richland, WA 99352, U.S.A., and funded by the U.S. Department of Energy. The Pacific Northwest Laboratory is a multiprogram laboratory operated by Battelle Memorial Institute for the U.S. Department of Energy under contract DE-AC06-76RLO 1830. Contact David Feller or Karen Schuchardt for further information.

(44) Biegler-König, F. W.; Bader, R. F. W.; Tang, T.-H. *J. Comput. Chem.* **1982**, *3*, 317.

(45) Biegler-König, F. *J. Comput. Chem.* **2000**, *12*, 1040.

(46) Paciorek, W. A.; Meyer, M.; Chapuis, G. *Acta Crystallogr. Sect A* **1999**, *55*, 543.

(47) Gervasio, G.; Bianchi, R.; Marabello, D. *Chem. Phys. Lett.* **2004**, *387*, 481.

(48) Espinosa, E.; Alkorta, I.; Elguero, J.; Molins, E. *J. Chem. Phys*. **2002**, *117*, 5529.

(49) Ponec, R.; Yuzhakov, G.; Sundberg, M. R. *J. Comput. Chem*. **2005**, *26*, 447.

(50) Gatti, C.; Bianchi, R.; Destro, R.; Merati, F. J. *Mol. Struct. (THEOCHEM)* **1992**, *255*, 409.

(51) Howard, S. T.; Hursthouse, M. B.; Lehmann, C. W. *Acta Crystallogr. Sect. B* **1995**, *51*, 328. (b) Volkov, A.; Abramov, Y. A.; Coppens, P.; Gatti, C. *Acta Crystallogr Sect A* **2000**, *56*, 332. (c) Henn, J.; Ilge, D.; Leusser, D.; Stalke, D.; Engels, B. *J. Phys. Chem. A* **2004**, *108*, 9442.

(52) Swaminathan, S.; Craven, B. M.; Spackman, M. A.; Stewart, R. F. *Acta Crystallogr., Sect. B* **1984**, *40*, 398. (b) Bianchi, R.; Gatti, C.; Adovasio, V.; Nardelli, M. *Acta Crystallogr., Sect. B* **1996**, *52*, 471. (c) Iversen, B.

B.; Larsen, F. K.; Figgis, B. N.; Reynolds, P. A. *J Chem. Soc., Dalton Trans.* **1997**, 2227. (d) Volkov, A.; Coppens, P. *Acta Crystallogr., Sect. A* **2001**, *57*, 395. (e) Bytheway, I.; Chandler, G. S.; Figgis, B. N. *Acta Crystallogr., Sect. A* **2002**, *58*, 451.

(53) Volkov, A.; Li, X.; Koritsanszky, T.; Coppens, P. *J. Phys. Chem. A* **2004**, *108*, 4283.

(54) Popelier, P. L. A. *Coord. Chem. Rev.* **2000**, *197*, 169.

(55) Bader, R. F. W.; Gillespie, R. J.; Martin, F. *Chem. Phys. Lett.* **1998**, *290*, 488.

(56) Bader, R. F. W.; Matta, C. F.; Cortés-Guzmán, F. *Organometallics* **2004**, *23*, 6253.

(57) Abramov, Y. A.; Brammer, L.; Klooster, W. T.; Bullock, R. M. *Inorg. Chem.* **1998**, *37*, 6317. (b) Farrugia, L. Mallinson, P. R.; Stewart, B. *Acta Crystallogr. Sect B* **2003**, *59*, 234. (c) Lee, J.-J.; Lee, G. H.; Wang, Y. *Chem. Eur. J.* **2002**, *8*, 1821. (d) Tafipolsky, M.; Scherer, W.; Öfele, K.; Artus, G.; Pedersen, B.; Herrmann, W. A.; McGrady, G. S. *J. Am. Chem. Soc.* **2002**, *124*, 5865.

(58) Gillespie, R. J.; Bytheway, I.; Tang, T.-H.; Bader, R. F. W. *Inorg. Chem.* **1996**, *35*, 3954.

(59) Macchi, P.; Proserpio, D. M.; Sironi, A. *J. Am. Chem. Soc.* **1998**, *120*, 13429.

(60) Farrugia, L. J.; Macchi, P. unpublished observations. The crystallographic site symmetry of the Co atoms in this compound is C_3, and the multipole populations were necessarily restricted by this symmetry.

(61) Although we find that the $4s^2 3d^8$ electron configuration provides the scattering factor with the best fit, the difficulties in determining the 4*s* population from charge density experiments are well-known (ref 17b). The very diffuse 4*s* density of the transition metal cannot easily be distinguished from diffuse density of the ligands.

(62) Lee, C.-R.; Wang, C.-C.; Chen, K.-C.; Lee, G.-H.; Wang, Y. *J. Phys. Chem. A* **1999**, *103*, 156. (b) Hwang, T.-S.; Wang, Y. *J. Phys. Chem. A* **1998**, *102*, 3726.

(63) Macchi, P.; Proserpio, D. M.; Sironi, A. *J. Am. Chem. Soc.* **1998**, *120*, 1447. (b) Note that Figure 3a in this reference is incorrect due to a program error (Macchi, P., personal communication).

(64) Wiberg, K. B.; Rablen, P. R. *J. Comput. Chem.* **1993**, *14*, 1504.

(65) Popelier, P. L. A. *Comput. Phys. Comm.* **1998**, *108*, 180.

(66) See for example ref 3o. (b) Bader, R. F. W.; Matta, C. F. *J. Phys. Chem. A* **2004**, *108*, 8385.

(67) Bultinck, P.; Vanholme, R.; Popelier, P. L. A.; De Proft, F.; Geerlings, P. *J. Chem. Phys. A* **2004**, *108*, 10359.

(68) We note that Cioslowski et al. (ref 3m) report an even smaller Bader charge for the Ni atom of 0.295.

(69) Spackman, M. *Chem. Rev.* **1992**, *92*, 1769.

(70) We choose here to quote the unabridged moments, rather than the traceless ones given in ref 15, since these are more directly comparable − see ref 69.

(71) Sabino, J. R.; Coppens, P. *Acta Crystallogr, Sect. A* **2003**, *59*, 127.